# Study of Microfluidic Mixing and Droplet Generation for 3D Printing of Nuclear Fuels

(2017)

PRÉSENTÉE LE 7 Sep 2017

À LA FACULTÉ DES SCIENCES DE BASE

PROGRAMME MASTER EN PHYSIQUE

ÉCOLE POLYTECHNIQUE FÉDÉRALE DE LAUSANNE

POUR L'OBTENTION DU GRADE DE MASTER ÈS SCIENCES

PAR

**Ahmed SHAMA**

acceptée sur proposition du jury :

Dr. Manuel Pouchon, directeur de thèse
Dr. Ivor Clifford, external examiner

ÉCOLE POLYTECHNIQUE
FÉDÉRALE DE LAUSANNE

Suisse
2017

# Acknowledgements

I appreciate and thank Dr. Manuel Pouchon for many things. Notably, for offering the research topic and the six months of stay in LNM/PSI under his supervision. Your encouragement and guidance are the reason we have this thesis. I also appreciate that you shared your experience and knowledge with me, and for your advices and discussions about this research and my career too. I hope that I have brought this research up to your expectations.

I am indebted to the LRS/PSI members who shared their experience and knowledge in CFD with me.

I also thank:

- Dr. Gina Oberbossel, for letting me measure the surface tension and contact angles of the fluids in the Institut für Verfahrenstechnik, ETHZ.

- Dominic Urban, for letting me perform the Taylor Dispersion Analysis in the labs of Adolphe Merkle Institute, University of Fribourg.

- Dr. Rühs Patrick, for letting me measure the rheology of the fluids in the labs of the Professorship Complex Materials, ETHZ.

I appreciate and thank Prof. Andreas Pautz and Prof. Horst-Michael Prasser. It is the contact with notable researchers like them that encourage and motivate persons who are taking their first steps in academia like me. They are the role models for many, including myself, and I have a hope that one day I could reach a part of what they are.

My friends Rachael and Aaron Colldeweih, they are great friends and family. I also thank their new born baby Lyla for behaving and being quite so that they managed to proof-read and correct my script in a professional way, I took the chance to permanently record this.

And of course my family; my parents, my sisters and my brother. I know you love me the most, and you have been always praying for me, I thank you for being with me.

# Abstract

Internal gelation and 3D printing processes were proposed to combine in a process that is promising to produce nuclear fuels with simplified production route and enhanced in-core performance [1]. The process relies on in-situ mixing of feed solutions that bear actinides and uranium nitrates with the methenamine and urea mixture. These feed solutions should be thoroughly mixed and kept at low temperature up to an inkjet printing head, where an inkjet printing process is used to deposit controlled volumes of the mixed solution on the pellet under-fabrication. Microwave and/or laser-heating are then used to trigger the gelation reaction and to solidify these printed dots and later to drive out the excess water and pre-sinter the gelled oxides.

The current study is an initial approach to optimize the upfront parameters of the 3D printing process. The feed solutions need be mixed in a passive microfluidic mixer, where the first optimization parameter is the minimum mixing time in the microfluidic mixer that will yield an acceptable mixing level. To do so, CFD modelling using OpenFOAM for different designs of microfluidic mixers was conducted to select the most efficient conception. To validate the CFD results, simulation of microfluidic mixers similar to some literature cases were performed and compared. The uncertainty of selected parameters in the CFD models was used to evaluate a conservative retention time and length. Secondly, the next printing step was modeled with OpenFOAM, which is the droplet generation process. The objective from these models was to correlate the feed parameters like the flow rate and the usage of an acoustic mechanical vibrator to the printed droplets size, generation rate, and the required stand-off distance of the printing head.

To perform these CFD simulations with the right solution parameters, rheology and diffusivity measurements were conducted. A proposed empirical approach was investigated for the evaluation of the diffusivity of multi-species solutions.

The resultant parameters from the current study are the mixing times and lengths for given microfluidic mixers that are industrially feasible, also, the rate and volume at which the droplets of the broth mixture are generated. These results can be used as guidelines for designing the inkjet printing head and to highlight areas where further investigations are required for an efficient production process.

# Keywords

Microfluidic Mixing, Droplets Breakup, 3D Printing, CFD, OpenFOAM

# Contents

**Acknowledgements** ..... I

**Abstract** ..... II

**Keywords** ..... III

**List of Figures** ..... VI

**List of Tables** ..... VIII

**List of Abbreviations** ..... IX

**Chapter 1. Introduction** ..... 1

1.1. The Scope of the Study ..... 2

**Chapter 2. Thesis Background (Processes)** ..... 4

2.1. The Internal Gelation Process for Nuclear Fuel Production ..... 4

2.2. The Microfluidic Mixing ..... 6

2.2.1. Quantification of the Mixing Efficiency ..... 8

2.3. The 3D Printing of Ceramics ..... 9

2.4. The Modes of Generating Droplets in 3D Printing ..... 10

**Chapter 3. Thesis Background (Numerical Solvers)** ..... 12

3.1. The OpenFOAM Software ..... 12

3.2. The underlying equations of the utilized numerical solvers ..... 13

3.2.1. The *twoLiquidMixingFoam* solver ..... 13

3.2.2. The *interFoam* and *interDymFoam* solvers ..... 14

3.2.3. The Turbulence Model ..... 15

3.2.4. The One Equation Eddy Viscosity Model ..... 15

**Chapter 4. Methodology** ..... 17

**Chapter 5. Experimental Measurements** ..... 19

5.1. The Rheology ..... 19

5.2. The Surface Tension ..... 21

5.3. The Contact Angles ..... 23

5.4. The Mutual Diffusivity ..... 24

5.4.1. The Theory of Taylor Dispersion Analysis ..... 24

5.4.2. The Apparatus ..... 26

5.4.3. The TDA Results ..... 27

**Chapter 6. Modelling of the Mixing Phenomenon** ..... 34
6.1. The Validation and Verification Case Studies ..... 34
6.1.1. The Specification of the Verification Models ..... 35
6.1.2. The Results of the Verification Models ..... 35
6.1.3. Assessment of the Verification Models ..... 36
6.1.4. Specification of the Validation Model of Microfluidic Mixing ..... 36
6.1.5. The Results of the Validation Models ..... 36
6.1.6. Assessment of the Validation Models ..... 37
6.2. 2D Modelling of the Microfluidic Mixers (Geometry Selection) ..... 38
6.2.1. Discussion of the 2D Modelling Results ..... 39
6.3. 3D Modelling of the Microfluidic Mixers (Mixing Parameters) ..... 40
6.3.1 Analysis of the 3D Micromixer Designs ..... 42
6.3.2. Mixing Enhancement in Winded Micromixers ..... 43
6.3.3. Mixing Enhancement in Multiple-Inlets Micromixers ..... 45
6.3.4. The Mixing Levels Downstream the Mixing Channel ..... 46
**Chapter 7. Modelling of the Droplet Generation Phenomenon** ..... 47
7.1. Specifications of the Inkjet Printing Head ..... 47
7.2. Physical Models of the Droplet Generation ..... 48
7.3. 2D Models of the Droplet Generation ..... 50
7.4. The Results of the Droplet Generation Modelling ..... 51
7.4.1. The Static Nozzles ..... 51
7.4.2. The Vibrating Nozzles ..... 52
**Chapter 8. Summary of The Design Parameters of the 3D Printing Head** ..... 54
**Chapter 9. Conclusions** ..... 55
**References** ..... 58

# List of Figures

Figure 1: A nuclear fuel production process that combines the IG and 3DP processes. The scope of the study is to investigate the reagents mixing and the droplet generation stages [2]. ..... 3
Figure 2: The KEMA type internal gelation flowsheet [5]. ..... 4
Figure 3: A simple "T" passive micromixer [10]. ..... 8
Figure 4: A Schematic diagram of a continuous inkjet (CIJ) printer (Left), and a drop on demand (DOD) inkjet printing system, where the middle is the thermal inkjet and ..... 11
Figure 5: The general structure of an OpenFOAM directory. ..... 13
Figure 6: A scheme of the current study. ..... 18
Figure 7: The viscosity of the CAN solution vs the shear rate. ..... 20
Figure 8: The viscosity of the HMUR solution vs the shear rate. ..... 20
Figure 9: The viscosity of the CAN, HMUR and the reference solutions at 5, 15, and 25 °C. ..... 21
Figure 10: The surface tension of the CAN and HMUR solutions at 18, 20, 22, and 25 °C. ..... 22
Figure 11: The surface tension of the reference solutions at 18, 20, and 22 °C. The surface tension can be interpolated as: $\gamma = 69.22 \pm 0.43\ [mN.m-1]$ at 20 °C. ..... 23
Figure 12: Droplets of the CAN solution ($H_{CAN}$ = 97.5° - 84.5° and $\theta_{CAN}$ = 89.9°). ..... 24
*Figure 13: Droplets of the HMUR solution ($H_{HMUR}$ = 106.7° - 87.9° and $\vartheta_{HMUR}$ = 94.4°).* ..... 24
Figure 14: A TDA data downstream of an injection point, after τ from the injection time [48]. ..... 25
Figure 15: The self-referencing detector (left) and the multi-pass capability of (right) of the TDA [58]. ..... 26
Figure 16: TDA of the HMUR into CAN at 8 °C along with functional bounds. ..... 30
Figure 17: TDA of the HMUR into CN at 16 °C along with functional bounds. ..... 30
Figure 18: The diffusivity of methenamine and urea into the CAN solution at 8 °C. Two empirical approaches are shown. The Gaussians superposition (±1σ) and the width-height technique. . 32
Figure 19: The diffusivity of methenamine and urea into the CAN solution at 16 °C. Two empirical approaches are shown. The Gaussians superposition (±1σ) and the width-height technique. . 33
Figure 20: The results of model II. The Y and Z velocity fields (Left), and a mid-section tracer (on vortices). ..... 36
Figure 21: The OpenFOAM results of the validation case. The fraction of species is shown at 5.65 mm from the mixing point, along with the 95% mixing criteria (left). The right horizontal plots correspond to the fraction of species at a mid-section cut (right) and the outside walls (left). 37
Figure 22: The double-T and double-wedge inlets. ..... 38
Figure 23: The seven models that were studied – (001) plane. ..... 39
Figure 24: The triple inlet micromixer (left, where the inlet of the metal solution is the middle, the HMUR is divided to two inlets) and the multiple inlets for the reference models. ..... 41
Figure 25: The mixing zone of the triple inlet micromixer (top, where the inlet of the metal solution is the middle, the HMUR is divided to two inlets) and the multiple inlets. ..... 41
Figure 26: The Prandtl flow is seen by observing the location of both solutions along the windings of the mixing channel (right), which shows the concentration of the solutions. The alternating behavior is not fully developed suggesting that higher winding radii may improve the mixing.

Prandtl flow is a 3D phenomenon, in which an axial component of the velocity is induced in alternating pattern between the different windings (left). ..... 44
Figure 27: Cross section view at the locations of winding direction change (first up to fourth change in winding direction), the CAN solution (blue) is alternatively shifting position to allocate itself around the high radius of the curvature and consequently displacing the slow HMUR solution. ..... 44
Figure 28: Cross section view at the first winding shift: 6.4 mL/min. The HMUR is detaching the right wall (right), to position itself in a lower curvature, such displacement will create an axial velocity ahead of the moving solution, where it is positive (up) in the top left part, and negative (down) in the bottom left part. ..... 44
Figure 29: The triple-inlet micromixer, where the “Red” represents the HMUR solution and the “Blue” represents the CAN solution. ..... 45
Figure 30: A cross-sectional cut downstream the mixing channel in the triplet inlets micromixer. An initial sharp gradient (left) develops into a softened gradient (right). ..... 45
Figure 31: A cross-sectional view of the downstream mixing channel of the triplet inlets micromixer. Initial vertically aligned interfaces are developing a curved shape by having a cross flow in the x and z directions. ..... 45
Figure 32: The NMI downstream the mixing channels in three of the modeled cases – for the winding mode, each point corresponds to the transition from a loop to another. ..... 46
Figure 33: The mesh of the 2D wedge geometry. The top section is the stationary mesh and the bottom is the dynamically oscillating mesh that represents an oscillating nozzle. The implemented boundary conditions are also shown. ..... 49
Figure 34: The range of parameters that are studied in the 2D droplet generation models: the frequency (horizontal), and the flow rate (vertical) – all the dimensions are in µm. The eight cases of the vibrating nozzle are labeled with Roman numerals. ..... 50
Figure 35: Droplets break-up as modelled in OpenFOAM from 100 and 250 µm static nozzles. Note that the image is not to scale in the axial direction. ..... 51
Figure 36: Droplets break-up as modelled in OpenFOAM from a 100 µm vibrating nozzle. Cases I, II, III, V, and VIII were modeled up to 5 mm, and the remaining cases are up to 10 mm. ..... 52

# List of Tables

Table 1: The average viscosity of the CAN, HMUR and the reference solution (x$10^{-3}$ [Pa.S]). ..... 21
Table 2: The TDA parameters for the three temperature measurements. ..... 26
Table 3: The density and the volume fractions of the two mixing solutions. ..... 27
Table 4: The weight (top) and molar fraction (bottom) of the CAN and HMUR solutions. ..... 27
Table 5: The diffusivities of methenamine and urea into the cerium ammonium nitrate at 8 and 16 °C - superposition of Gaussians distributions. ..... 31
Table 6: The diffusivities of methenamine and urea into the cerium ammonium nitrate at 8 and 16 °C - correlating the width of the distribution to the fractional height. ..... 31
Table 7: The Einstein-Stokes's equation for the diffusivities - superposition of Gaussians. ..... 31
Table 8: The Einstein-Stokes's equation for the diffusivities - correlating the width of the distribution to the fractional height. ..... 31
Table 9: The dimensions and flow characteristics in the validation case studies [10]. ..... 35
Table 10: The velocities of the verification models [10], and the results of the OpenFOAM simulations (right column). ..... 35
Table 11:The NMI and the pressure drop from the selected seven geometries. ..... 39
Table 12: The specifications of the six modelled microfluidic mixers. The winding radius is 1 mm except for the scaled geometry No 5, which equals 2 mm. ..... 40
Table 13: The dimensionless numbers governing the mixing phenomena. ..... 41
Table 14: The mixing times and lengths to achieve the required mixing levels (-5.0% and -2.5%) from the perfectly mixed conditions. ..... 43
*Table 15: The break-up diameter and time for the static nozzles.* ..... 51
Table 16: The droplets break-up diameters, times and the nozzle stand-off distances for the vibrating models. ..... 53

# List of Abbreviations

| | |
|---|---|
| 3DP | Three Dimensional Printing |
| AC | Actinides |
| ADUN | Acid Deficient Uranyl Nitrate |
| AI | Absorption Index |
| AM | Additive Manufacturing |
| CAN | Cerium Ammonium Nitrates |
| CFD | Computational Fluid Dynamics |
| CIJ | Continuous Inkjet Printing |
| DOD | Drop on Demand (Inkjet printing) |
| DIP | Direct Inkjet Printing |
| FVM | Finite Volume Method |
| GNU | General Public License |
| GUI | Graphical User Interface |
| HMTA | Hexamethylenetetramine (Methenamine) |
| HMUR | The Methenamine and Urea Mixture |
| HPLC | High Precision Liquid Chromatography |
| IG | Internal Gelation |
| KEMA | Keuring van Elektrotechnische Materialente Arnhem (a nuclear fuel wet production route) |
| LES | Large Eddy Simulation (Turbulence Model) |
| LWR | Light Water Reactor |
| MA | Minor Actinides |
| MF | Microfluidic |
| MFM | Microfluidic Mixer |
| MI | Mixing Index (a measure of the mixing efficiency) |

| | |
|---|---|
| NMI/RMI | Normalized Mixing Index (a flow rate independent measure of the mixing efficiency) |
| NSI | Normalized Segregation Index (a flow rate independent measure of the mixing efficiency) |
| OM(x) | The x's Order of Magnitude |
| OpenFOAM | Open Field Operation and Manipulation (an open source CFD Software) |
| PDE | Partial Differential Equation |
| RANS | Reynolds Averaged Navier-Stokes Equations |
| RAS | Reynolds Average Stress (Turbulence Model) |
| RP | Rapid Prototyping |
| SGS | Sub-grid Scale (LES model type) |
| TAC | Total Actinides |
| TDA | Taylor Dispersion Analysis |
| TRISO | Tristructural-Isotropic (nuclear fuel particles) |
| VOF | Volume of Fluids |
| VHTR | Very High Temperature Reactor |

# Chapter 1. Introduction

Generation IV nuclear reactor concepts have many advantages over current reactor designs, which include the fuel cycle closure and enhanced safety features. The former is related to the transmutation of actinides (AC), minor actinides (MA) and even repository relevant radiotoxic fission products. The latter is related to the enhanced operational safety and accident tolerances. These objectives are also related to the nuclear fuel itself not only the reactor design. Therefore, major research and development of Gen IV reactors was undertaken to design nuclear fuels which fulfill these objectives. It is for example a goal to design a fuel with increased loading of the total actinides (TAC) for both increased conversion and reduction of the final waste radiotoxicity. Furthermore, stricter requirements of the nuclear fuel element integrity during operational and accident conditions are required.

An innovative approach for the nuclear fuel production is proposed by Pouchon [1] which could enhance the previously mentioned features of the inclusion of MA for transmutation and the fuel safety characteristics, especially during production, but also in the reactor. In the proposed approach, the well-established internal gelation process (IG) is combined with the 3D ceramic printing (3DP). The IG process is a wet process for production of microspheres of metal oxides, carbides, and other chemical forms. The process is suitable for nuclear fuel concepts like the sphere-pac and the TRISO fuel kernels that could be operational in Gen IV reactors like fast systems and the VHTR. The ceramic 3DP is an additive manufacturing technique (AM) in which a green body is built from a feed solution containing ceramic particles in a suspension. In the combined process, two modifications were proposed. First, rather than feeding the 3DP printing head with a suspension, a feed solution that can harden later by heat application is utilized which integrates the IG into 3DP. In this case, the mixture of the metal nitrates with the methenamine and urea solution having the ability to gel by heat. Second, the already tested microwave heating will be used to trigger the gelation reaction and drive out the excess fluids from the printed droplets. The microwave energy is used instead of heating in a silicon oil bath. In parallel to drying, a laser will initiate the sintering of the under-construction nuclear fuel pellet. The process is schematically represented in figure 1.

This nuclear fuel production process has the advantage of being a wet process, which promises to be almost powderless. Powderless techniques are favorable for AC and MA bearing fuels which require shielded and remote production units. Additionally, the 3DP approach has the advantage of local compositional control, hence the final fuel pellet will have local features that will enhance the in-core performance and accident tolerance (by introducing for example buffer and silicon carbide isolation layers) [2]. These two advantages will also help to realize fuel pellets that bear a spatially controlled loading of MA and AC for transmutation purpose and for fuel cycle closure [1].

Nevertheless, nuclear fuel pellets must be produced on a mass scale (a typical 1GW LWR consumes ~6 million pellets in a single refueling). A successful fuel production process must be suitable for mass production, and combining two processes with their own complexities and requirements poses the possibility of high fuel pellets rejection rates during the production. Consequently, there would likely be an increase in the maintenance requirements and failure rates of the production equipment, which is disadvantageous in production of AC and MA bearing fuels. The combined production process must be investigated and optimized in a way that enhances both the efficiency and reliability in order to deem it suitable for mass production of nuclear fuel pellets.

## 1.1. The Scope of the Study

The scope of the study is to investigate upfront stages in the production process; the reagents mixing and the droplet generation (figure 1). The final production stages like the sintering could require special inputs (particle size and distribution) that will only yield an acceptable fuel pellet quality. Therefore, the upfront stages under study will be investigated as a function of ranges of parameters that can yield acceptable output to the downstream production stages, allowing an overall optimized production process.

In the reagent mixing stage, the aim is to thoroughly mix the reagents while suppressing the IG reaction up to the printing head. Therefore, the first objective is to optimize the design of the microfluidic mixer by selecting between different proposed geometries to minimize the mixing time and length while yield an acceptable mixing index at the same time. CFD modeling using OpenFOAM is used for this stage. Yet, validation of the CFD models with similar cases from literature was conducted first and foremost. Propagating the experimental errors of the diffusivity and viscosity values was performed to estimate a conservative mixing time and mixing length.

In the droplet generation stage, the objective is to control the process spatially and temporally, by having a controlled droplets generation rate, with a controlled size. Additionally, to minimize the droplets size to enhance the spatial resolution in the green pellet that is under fabrication. The objective in this stage is to evaluate the droplets size and generation rate from a vibrating and a non-vibrating printing head. CFD modelling using OpenFOAM is used for this purpose. To perform these CFD simulations, specific properties of the fluids needed to be evaluated. Therefore, measurements that address the rheology and diffusivity of the fluids under study were performed.

The study will recommend the design parameters of a 3DP head that is feed with the IG mixtures. The parameters are the microfluidic mixer design, flow rates, and the specification of the vibrating nozzle that should yield an acceptable product for the next 3DP stages of the nuclear fuel pellet.

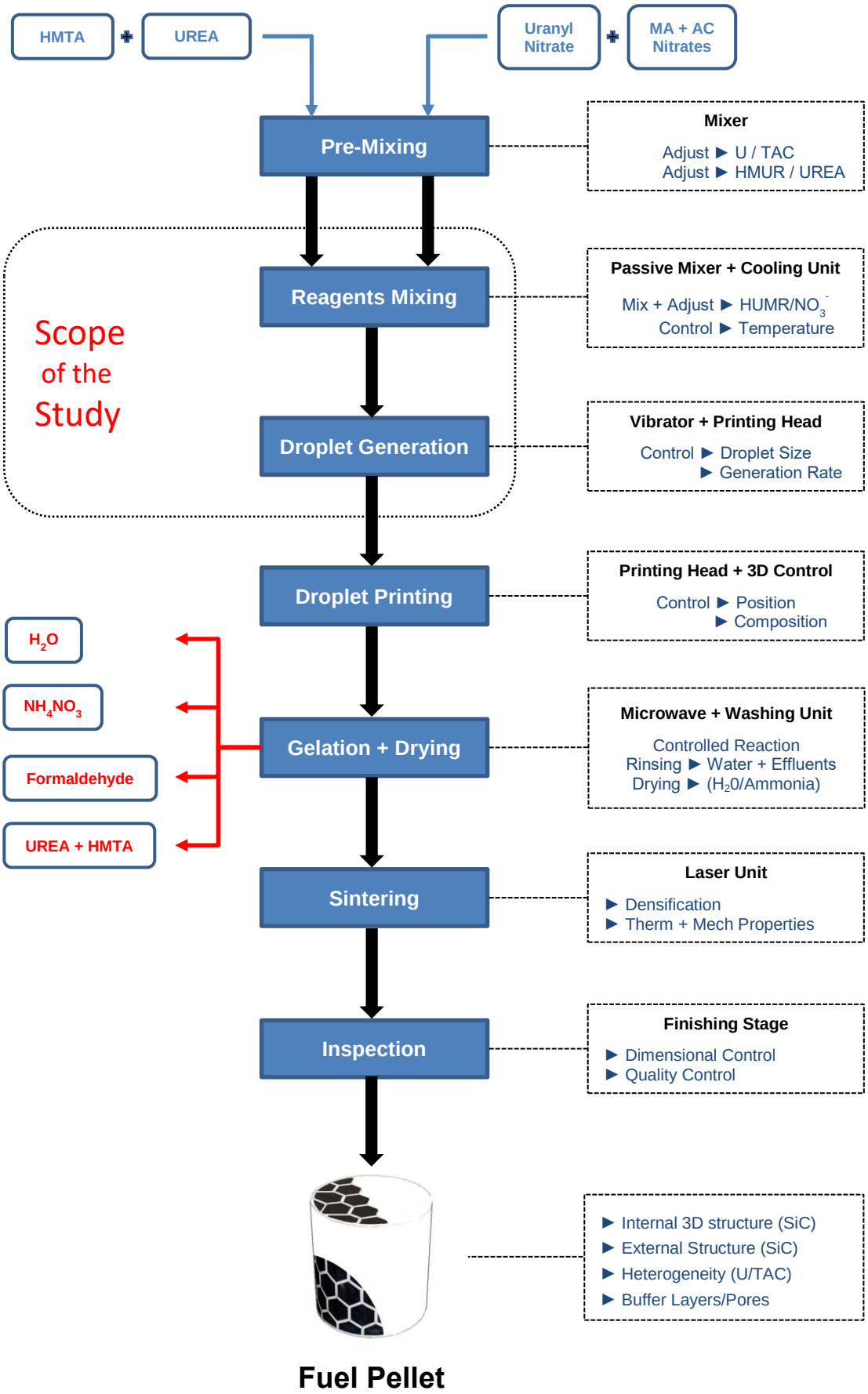


*Figure 1: A nuclear fuel production process that combines the IG and 3DP processes. The scope of the study is to investigate the reagents mixing and the droplet generation stages [2].*

# Chapter 2. Thesis Background (Processes)

## 2.1. The Internal Gelation Process for Nuclear Fuel Production

In the nuclear fuel production, gelation is a sol-gel process that produces microspheres of hydrous metal oxides ($UO_3.H_2O$) [3] [4] as termed "*the KEMA process*" [3] with sizes between 30 and 1200 μm [5]. A flow chart of the process is shown in figure 2. Later, these microspheres are used as kernels for the TRISO nuclear fuel for the pebble bed type reactors or in the fabrication of the sphere-pac type fuel [6]. The preferred application will be the fast spectrum reactors like the SFRs that have high MA transmutation characteristics. The process has gained interest since it is powderless, starting from the uranyl nitrate solution, which could be either prepared by the dissolution of the metal oxide in nitric acid or directly as an outcome of the fuel reprocessing. For this reason, it is suitable for fuel that is meant for transmutation, and which therefore bears considerable amounts of AC and MA [3] [7]. Such fuel requires complex handling and safety consideration if present in a powder form during the production. Additionally, the sol-gel process has been improved through the internal gelation (IG) technique [5] realized with microwave heating [8], resulting in a further simplification of the process. It is also capable for a high production rate with a precisely controlled size, enabling its usage for the sphere-pac concept fuel which requires at least two size fractions.

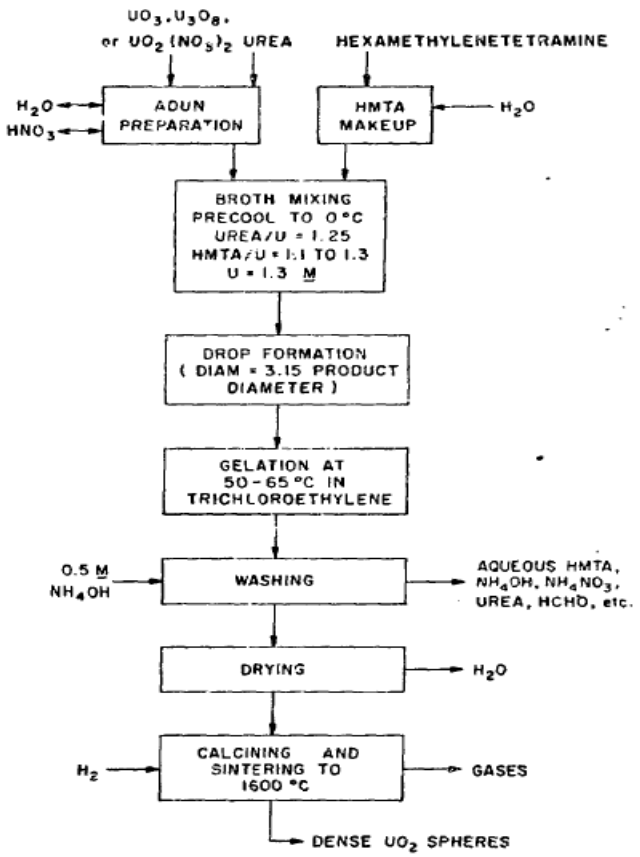


*Figure 2: The KEMA type internal gelation flowsheet [5].*

The starting broth is a thoroughly mixed and cooled mixture of acid deficient uranyl nitrate (ADUN) $UO_2(OH)_{0.5}(NO_3)_{1.5}$ and a solution of methenamine (HMTA) $C_6H_{12}N_4$ and urea $CH_4N_2O$ [4] [5] [9], which must be kept at a temperature from 0 to 5 °C. Typical molarities are: 3.18 M HTMA, 3.18 M urea and 1.675 M cerium ammonium nitrate [4]. To study the IG process, cerium ammonium nitrates (CAN) $[(NH_4)_2Ce(NO_3)_6]$ can be used as a substitute for uranyl nitrates during the internal gelation [4], hence, it is the metal bearing solution used in the current study. The mixture is temperature sensitive and should be kept cool to be stable (no gelation). The generated droplets of the mixture are then heated up to a temperature range between 45 and 90 °C, where the solution decreases in acidity (pH<7) and $Ce^{4+}$ salts precipitate, driven by the release of ammonia from the HTMA decomposition. The following reactions take place sequentially leading to homogenous gelation throughout the droplets [9] [5]:

***Complexation/de-complexation*** *– Urea complexes the metal ions at low temperature and prevents the premature precipitation, by temperature rise, the reverse reaction (de-complexation) occurs.*

$$2CO(NH_2)_2 + Ce^{4+} \leftrightarrow Ce[CO(NH_2)_2]_2^{4+}$$

***Hydrolysis*** *– The decomplexation of urea drives the hydrolysis reaction of cerium – hydrous cerium oxides are final products of this gelation process.*

$$Ce^{4+} + xH_2O \leftrightarrow Ce(OH)_4{\bullet}yH_2O_9 + 4H^+ \qquad \text{and} \qquad CeO^{2+} + xH_2O \leftrightarrow CeO(OH)_2{\bullet}yH_2O_9 + 2H^+$$

***HMTA protonation*** *– The protonation of HMTA by a single H cation makes the solution basic (pH<7) and drives the cerium hydrolysis reaction. This reaction is catalyzed by the presence of urea.*

$$(CH_2)_6N_4 + H^+ \leftrightarrow (CH_2)_6N_4{\bullet}H^+$$

***HMTA decomposition*** *– The protonated HMTA starts to decompose, removing additional H cations and increasing the basicity, which leads to effluents of formaldehyde and ammonium nitrates. Formaldehyde and ammonium hydroxide are the reactants for preparation of the HMTA.*

$$(CH2)_6N_4{\bullet}H^+ + 3H^+ + 6H_2O \leftrightarrow 4NH_4^+ + 6CH_2O.$$

The kinetics of these reactions is controlled by the chemistry of the feed solutions (ADUN molarity, HMTA/$Ce^{4+}$ and $OH^-/Ce^{4+}$) and the decomposition rate of HMTA, the deposition rate of the oxides and the rate of heat transfer [5]. It is essential to provide a sufficient (HMTA/$NO_3^-$) ratio to have enough HMTA decomposition per nitrate molecules [4]. Also, the gelation reaction is temperature-driven, so, droplets of the broth mixture are heated up in a column of a hot immiscible organic medium, usually silicon oil, trichloroethylene or in a microwave cavity, which is an advanced approach, where the immiscible organic medium is avoided. The contact-less microwave approach is advantageous because the waste fluid for heating and washing are minimized. The gelation temperature ranges between 50 and 75 °C to yield good gel properties, and the gelation time range

from <1 sec to several minutes depending on the gelation temperature, and if the heating oil from the surface or volumetric (microwaves). The following stage is washing of the reaction products (usually with ammonium hydroxide) which are: ammonium nitrates, formaldehyde and excess urea and HMTA. Then drying and calcination to remove the excess water and ammonium nitrates. And at last, a sintering stage is performed for the required densification. The resulting products are ceramic microspheres of the metal oxides for usage as nuclear fuel [4].

The resultant properties of the gel particles depend on the reaction temperature and the chemistry of the broth [5]. The production of the gel particles is practical where premature gelation in the broth is avoided. Therefore, the objective in this study is to prevent the premature gelation in the microfluidic mixers, and therefore to minimize the mixing time and the time from the initial mixing to the droplet formation, where the product leaves the tubes. Also, the gelation temperature must be below the boiling point of the broth to prevent the formation of vapor bubbles. This represents a major step that requires further investigations (gelation and drying). In addition, successful washing up of the effluents without disturbing the gelled structure being formed requires further research. The main difficulty is that the washing agent to gel volume is large (an order of magnitude or more). Additionally, it will be required to control the required time to wash the effluents from the gelled structure (this time scale is in minutes). Washing is a mass transfer process that is diffusion controlled, and it is required to yield acceptable properties of the gelled. Lastly, drying could be achieved through microwave heating to drive out the excess water and ammonium nitrates.

## 2.2. The Microfluidic Mixing

The first process under study is the mixing of the CAN to the HMTA and urea mixture. In the production process, CAN will be replaced with a mixture of uranyl nitrate and a controlled fraction of the total actinides. Once the reagents are mixed, the broth is stable for a limited time depending on the temperature. Usually it is cooled between 0 and 5 °C, but introducing the actinides in the broth provide be an internal heat source, in addition to the heat from the flow of the broth in the channels up to the printing head (due to friction). The scope of the current work is to find the design parameters of the microfluidic mixer that will minimize the mixing time up to the printing head. Also, for production of gel particles with acceptable properties, the reagents are mixed to a sufficient level before the gelation reaction could be initiated. Insufficient mixing will result in inhomogeneous properties and unsatisfactory gelled particles, or even no reaction at all. Therefore, the mixing level must be be high enough for practical applications. Additionally, minimizing the retention time in the microfluidic mixers, the extent of gelation in the miniature channels that are prone to blockage is lower. Blockage must be avoided in the production process since that would imply production downtimes and maintenance activities for equipment that handles radiotoxic actinides.

Macro mixers are not promising in the current application, given that the mixing times for the active/passive microfluidic mixers are on the order of milliseconds. Also, these mixers have dead volumes where the fluids can reside and later gel into oxides and result in a permanently contaminated mixer. Micromixers on the other hand can be designed to have open flow channels that are less probable to stagnate the flow. Also, the miniature size of the micro mixers will exclude the criticality issue of the metal nitrate solution and could be easily implemented as integral parts on the proposed inkjet printing head, which is the next process in the current production approach. For these reasons, passive microfluidic mixers were investigated for the sake of efficient mixing in a rapid manner.

Micromixers can be classified into two categories: active and passive. Active micromixers require an external force to perform their function, for example dielectric, magnetic or ultrasonic to stir, perturb and create complex flow fields and hence mixing will be enhanced. Even faster than macro-mixers, active micromixers do not achieve the required mixing index fast enough compared to the passive ones [10]. Additionally, the induced forces, for instance acoustic vibrations, will generate considerable heating in the mixer, leading to a temperature rise of 15 °C or more, and therefore to potentially undesirable effects. On the other side, passive mixers do not rely on external forces except for the pressure that drives the flow. Passive micromixers have a low Reynolds number and the flow is dominantly laminar so turbulent mixing is not evident, instead they rely on the molecular diffusivity when the reagents comes into contact. Their main advantage is the rapid mixing of the solutions. A tee micromixer is shown in figure 3 [10]. The underlying principle of passive mixers is the Fickian diffusion, which scales with the diffusion time and is inversely proportional to the squared diffusion distance. Diffusion time is reduced by increasing the contact time and minimizing the diffusion distance through special geometrical effects [11]. Fick's first law of diffusion can be written as [12]:

$$J_i = -D_{ij}\,\nabla\varphi_i \qquad \textit{Equation 1}$$

Where $\boldsymbol{J_i}$ is the diffusion current (only concentration driven without convective transport), or the number of moles of component $\boldsymbol{i}$ that flow through a unit area in a unit of time [$m^{-2}s^{-1}$]. And $\boldsymbol{D_{ij}}$ is the Fickian diffusion coefficient of component $\boldsymbol{i}$ into component $\boldsymbol{j}$, or vice versa [$m^2s^{-1}$]. And $\boldsymbol{\varphi_i}$ is the molar concentration of the component $\boldsymbol{i}$ [$mol.m^{-3}$].

Several approaches are reported in literature to enhance the efficiency of passive micromixers:

- By inducing inertial forces that create flow separation, as evident in zigzag micromixers [13].
- By inducing shear forces between the two species that flow at different speeds [14].
- By creating complex 3D geometries that enhanced the advection effect [15].
- By sequentially splitting and recombining the flow channel [16].
- By using static mixing elements that abruptly change the flow channel cross section [17].
- By creating a narrow section in the micromixer that brings the two reagents very close [18].

Other designs of both active and passive principles are reported in the literature [11].

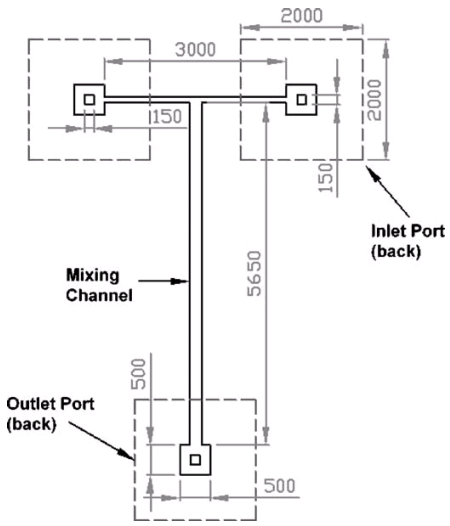


*Figure 3: A simple "T" passive micromixer [10].*

### 2.2.1. Quantification of the Mixing Efficiency

In the current study, the parameter of interest is the mixing time to achieve a certain level of mixing. For quantifying the level of mixing in a micromixer, "*Mixing indices*" will be used. Mixing indices are a measure of the standard deviation of the concentration of species at specific cross sections, and the following index was selected from the literature:

***The Relative Mixing Index (RMI)*** [19]***:***

$$RMI = 1 - \frac{\sigma}{\sigma_a} = 1 - \frac{\sqrt{\frac{1}{N}\sum_{i=1}^{N}(I_i - \langle I \rangle)^2}}{\sqrt{\frac{1}{N}\sum_{i=1}^{N}(I_{unmixed,i} - \langle I \rangle)^2}} \qquad \textit{Equation 2}$$

Where $\boldsymbol{\sigma}$ is the standard deviation of the concentration (or the fraction of species $\boldsymbol{i}$) at a specific location, and $\boldsymbol{\sigma_a}$ is the standard deviation of the fully unmixed condition. $\boldsymbol{I}$ is the local concentration or fraction of species $\boldsymbol{i}$ (for $\boldsymbol{N}$ cells in simulation or $\boldsymbol{N}$ pixels in optical measurements of the mixing). $\langle \boldsymbol{I} \rangle$ is the average pixel intensity or species concentration at the cross section. The ***RMI*** between from 0 to 1, where an NMI that equals 0 implies a fully unmixed state, and an NMI that equals 1 implies full mixing. The reverse index (***1- RMI***) would represents the index of segregation.

***Volumetric Fraction of Species (Alpha):***

When the two fluids have different flow rates $\boldsymbol{F_a}$ and $\boldsymbol{F_b}$ (as the fluids in the current study), full mixing can be obtained where the volumetric fractions $\boldsymbol{a}$ across the channel can be represented as:

$$\alpha = \frac{F_a}{F_a + F_b} \qquad \textit{Equation 3}$$

Such requirement is not guaranteed to be achieved in all the micromixer designs that are proposed in the current study. For this reason, the 2.5% and 5.0% deviation from this ratio will be monitored downstream of the mixing channel, which corresponds to 97.5% and 95% mixing levels, respectively.

## 2.3. The 3D Printing of Ceramics

To our knowledge, nuclear fuel such as $UO_2$ (as a ceramic part) has not been reported in literature to be printed before. Even, 3D printing has been implemented for components in a nuclear power plant for the first time in 2017, as announced by Siemens [20] with the 3D printing of a pump impeller. Such a breakthrough gives the potential for other components to be 3D printed and licensed to operate, including the nuclear fuel itself.

The traditional production processes of nuclear fuel pellets for current Gen-III LWR's is a dry powder-based technology. The upcoming Gen-IV nuclear reactors concepts will rely on a nuclear fuel that bears considerable amounts AC and MA for transmutation and the closure of nuclear fuel cycle over plutonium or over plutonium and minor actinides. Such nuclear fuel composition would complicate the production process of the nuclear fuel pellets, due to the dust generation and the subsequent radiological measures during the manufacturing process (hot cells, remote handling, etc). As proposed by Pouchon [1] [2], a nuclear fuel production approach that is based on a full wet-route could be advantageous for such an application. The approach relies on combining a ceramic production process (the internal gelation) with an additive manufacturing process (inkjet printing of ceramic parts).

Generally, 3D ceramic parts with complex geometry and controlled internal structure and composition can be fabricated using an additive manufacturing (AM) or rapid prototyping (RP), which are incremental processes, and they are described by Sachs et al. from MIT, US [21], and later by Xiang et al. from Brunel university, UK [22], and Shao et al. [23]. The common approaches in this AM processes are three dimensional printing (3DP) [24] and direct inkjet printing (DIP) among other approaches.

These processes rely on the usage of a printing head (contactless), and through which a slurry (a powder suspension or a pigment in a liquid or carrier) is being deposited on the under-construction green part. The printing head is used to: dispense and break the liquid stream into controlled volumes of droplets (droplet generation), position the droplets on a surface, and solidify these droplets [22]. Solidification is achieved through evaporating the carrier fluid or the binder that is mainly acting as an adhesive [25] [26], leaving behind a dense paste of the micro ceramic powder. Successive layers are deposited for construction of the final green body as in typical additive manufacturing. Additionally, parallel inkjet printing of slurries with different compositions can be implemented, as in the typical multi-color inkjet printing heads. Final sintering phase will follow for the required densification.

Generally, the feed liquids for the inkjet printer can be categorized as either a solution or a suspension. Both comply with certain requirements for successful implementation, namely the ability to solidify after printing.

The major difficulty in ceramic inkjet printing with slurries is the possibility of blockage of the printing head, leading to production downtimes, also the fluid behavior, which affects the final quality of the ceramic part. The former will have a special consideration in nuclear fuel production that bears AC and MA, which would increase the waste volumes and the production time. A former approach combined the 3DP with the gelation process to produce a Zirconia green body, in which the gelation process was used to produce Zirconia powder (<0.5 μm) suspended in a solution that was used later in the printing process through an extrusion module into the green body under fabrication [23]. On the contrary, as proposed by Pouchon and Streit [27], using a fluid instead of a slurry will eliminate the associated blockage difficulty. This fluid solidifies later on the surface; hence the gelation process produces the required viscosity of the printed droplets for maintaining a stable shape up to the drying stage. The complexity of the later approach (which is the scope of the current study) is the elimination of the reaction effluents from the solidified droplets (between 75 and 80%) as compared to the gel extrusion performed by Shao et al. [23]. In the work of Shao et al. [23], the effluents and the solid fractions were ~50% each, and the effluents were mostly water. Another difficulty for the later approach arises from the fact that the internal gelation effluents are mainly excess HMUR, ammonium nitrates, urea, and other compounds which are solids dissolved in the excess water, hence, not only a drying process will be insufficient, a washing process must be applied or applying an alternative evaporation/ incineration processes. Further investigation for the washing and drying stages are necessary to result in comparable process quality control to that of the already established printing of slurries.

## 2.4. The Modes of Generating Droplets in 3D Printing

3D printing of ceramic parts requires generating and precisely positioning controlled volumes of the fluids of interest on the under-construction green body. The control of the volume of the generated droplets and their accurate positioning is affecting the spatial resolution of the final ceramic part, and since the process under study is to build a fuel pellet with internal features, controlling the resolution is advantageous to the overall process quality.

The common approaches for generating the droplets in a printing head are the continuous inkjet printing (CIJ) and the drop-on-demand inkjet printing (DOD) [25] [28], and both can generate droplets between 10 to 150 μm [25]. The CIJ method relies on the breakup of the pressure driven liquid column by the Rayleigh instability, to form droplets that are generally larger than the nozzle diameter. The DOD method which is popular in inkjet printing of ceramics, relies on a piezoelectric actuator [29] to create a pressure pulse in the upstream fluid behind the printing nozzle [25] (figure 4).

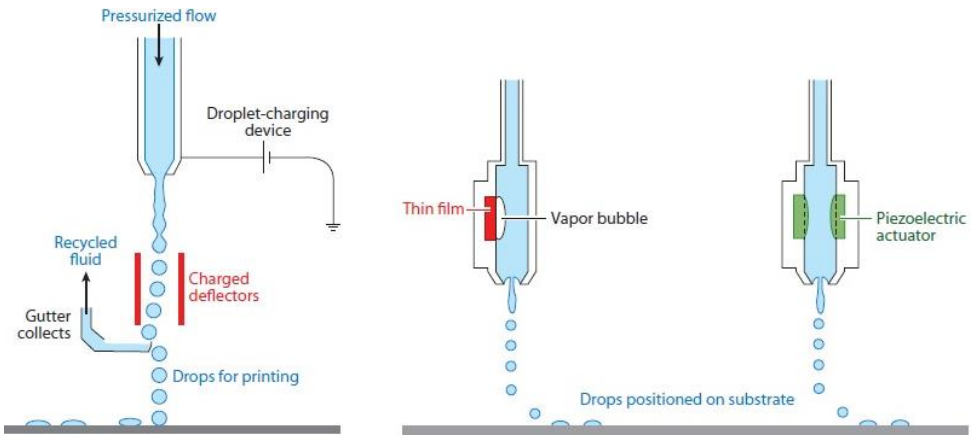


*Figure 4: A Schematic diagram of a continuous inkjet (CIJ) printer (Left), and a drop on demand (DOD) inkjet printing system, where the middle is the thermal inkjet and the right is the piezoelectric inkjet [29].*

As will be explained in chapter 7, the flow rates of interest resulted in either a continuous fluid column or a delayed breakup by Rayleigh instability. For spatial resolution purpose, it is envisioned that the printing head will be located 4-5 mm ahead of the under-construction pellet. For this reason, another droplet generation approach was studied, which is to assist the premature liquid column breakup by mounting the printing head on an acoustic vibrator.

As explained by Huimin Liu [30], acoustic atomization is a division of “Vibration Atomization”. The process relies on assisting the breakup of the liquid by explicitly imposed periodical vibration on the liquid column or in the upstream reservoir. In a previous study by Pouchon et al [27], a shaker that has up to 13 KHz vibration frequency was used to generate a continuous and stable droplets stream of the CAN and HMUR mixture (which will be investigated in the current study). The liquid jet is naturally unstable, and eventually, introducing the acoustic vibration will result in a premature breakup of the liquid jet, which depends on the nozzle diameter, vibration frequency, amplitude, flow rate and the fluid properties. The effects of various process parameters on the jet breakup will be studied for this purpose.

# Chapter 3. Thesis Background (Numerical Solvers)

The physical phenomena of interest in the current work are mixing of two incompressible and miscible fluids and droplets breakup from a needle nozzle. The first phenomenon is modelled with the OpenFOAM software (V4.1) on an Ubuntu 16.10 machine, using the *twoLiquidMixingFoam* solver, and the latter is modelled using the *interFoam* and *interDymFoam* solvers. The following sections describes the physical models and the underlying governing equations.

## 3.1. The OpenFOAM Software

OpenFOAM (Open Field Operations and Manipulations) is an open-source CDF software family that is developed by OpenCFD Ltd. [31] and distributed by the OpenFOAM foundation [32] under the GNU General Public License. The numerics of OpenFOAM are based on the finite volume method (FVM) of solving coupled sets of algebraic equations. The equations are spatially and temporally discretized PDE's governing systems of equations (conservation equations) on a grid. The grid represents the computational domain, which can be structured or unstructured and also moving or fixed. In the current work, the grids are stationary for the microfluidic mixing, and moving for the 3D printing models. The main steps in approaching a CFD problem are described in the following points:

***1. <u>Mesh Generation</u>***

In generating a mesh, a computational domain is defined and partitioned into smaller and non-overlapping cells on which the numerical solver will solve for the field values on cells or cell surfaces. In the current work, several geometry and meshing tools were used. The first tool used was SALOME [33], which is an open-source software developed by OPEN CASCADE. Secondly, a trial version of TRELIS [34], which is a commercial software that was used to mesh the micromixer models. The last tool used was *blockMesh* mesh generation utility (supplied with OpenFOAM) [35]. As will be discussed in section 4, the numerical solution itself should be independent on this grid specification, and the grid should be suitable for the fields description by local refinement, boundary layers, etc.

***2. <u>Data Preparation</u>***

The input data for OpenFOAM must be organized in a main directory, as shown in figure 5. The *system* directory contains the properties of the solver such as: steady-state or transient, time integration, interpolation, discretization schemes, coupling algorithm, etc. The time directories contain

the field values such as pressure, velocity, and phase fractions, including the initial field values and the boundary conditions. The *constant* directory contains the physical properties, turbulence model, mesh dynamics, and a subdirectory for the mesh specification (*polyMesh* sub-directory).

***3. Numerical Solver***

A numerical solver is required to solve the generated set of discretized and approximated PDE's, hence, the solution is numerically, approximated and discretized. The utilized numerical solvers are: *twoLiquidMixingFoam, interFoam* and *interDymFoam* for the mixing and droplet generations cases. The underlying equations are detailed in section 3.2.

***4. Post-Processing***

The post processing tool utilized in the current work is *paraView/paraFoam* graphical user interface (GUI) that is provided with OpenFOAM [36].

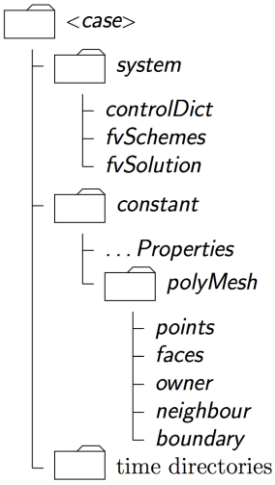


*Figure 5: The general structure of an OpenFOAM directory.*

## 3.2. The underlying equations of the utilized numerical solvers

The current models address an incompressible, isothermal, and Newtonian flow. The set of equations that are solved (after discretization, integration, and approximation) by the selected solvers are: a mass continuity equation, a set of Navier-Stoke's equations and a turbulence model specific equation. Additionally, a diffusivity equation is required for the mixing phenomenon and phase continuity equation for the droplet generation phenomenon.

### 3.2.1. The *twoLiquidMixingFoam* solver

The *twoLiquidMixingFoam* is a transient, isothermal solver for mixing of two miscible and incompressible fluids, which solves the discretized PDE's that represent the diffusivity and convection driven mixing between the two fluids. Two turbulence models were used along with the solver (laminar and LES). The following equations are the underlying PDE's for laminar flows:

Continuity equation – for incompressibility constraint

$$\nabla . \boldsymbol{U} = 0 \qquad \textit{Equation 4}$$

Momentum equations – for momentum transport

$$\frac{\partial \rho \boldsymbol{U}}{\partial t} + \nabla . (\rho \boldsymbol{U}\boldsymbol{U}) = -\nabla p_{rgh} - \boldsymbol{g} h \nabla \rho + \nabla . \boldsymbol{\tau} \qquad \textit{Equation 5}$$

Diffusivity equation – for transport of species

$$\frac{\partial \alpha}{\partial t} + \nabla . (\rho \boldsymbol{U} \alpha) = \nabla . (\left[D + \frac{1}{S_c} D_t\right] \nabla \alpha) \qquad \textit{Equation 6}$$

Where;

$$\boldsymbol{\tau} = -\frac{2}{3}\mu_{eff}(\nabla . \boldsymbol{U})\boldsymbol{I} + \mu_{eff}[\nabla \boldsymbol{U} + \mu_{eff}(\nabla \boldsymbol{U})^T] \qquad \textit{Equation 7}$$

$$\rho = \alpha \rho_1 + (1 - \alpha)\rho_2 \qquad \textit{Equation 8}$$

$$\mu_{eff} = \alpha \mu_1 + (1 - \alpha)\mu_2 \qquad \textit{Equation 9}$$

Where $\boldsymbol{U}$ is the mixture velocity, $\boldsymbol{\alpha}$ is the phase fraction of the first species, $\boldsymbol{\rho}$ is the fluid density, $\boldsymbol{p}$ is the pressure, $\boldsymbol{D}$ is the mutual diffusivity between the two species, $\boldsymbol{D_t}$ is the turbulence driven molecular diffusivity, $\boldsymbol{S_c}$ is the Schmidt number, $\boldsymbol{\mu}$ is the dynamic viscosity and $\boldsymbol{\tau}$ is the stress tensor. The Newtonian nature of the flow was evident in rheology and will be further discussed in the experimental measurements (chapter 5).

### 3.2.2. The *interFoam* and *interDymFoam* solvers

The *interFoam* and *interDyMFoam* solvers are incompressible, transient, and isothermal solvers for two immiscible fluids using the volume of fluid (VOF) phase fraction for tracking the interface between the two fluids. The *interDymFoam* is the original *interFoam* with a dynamic mesh option (either motion or topology). The *interDyMFoam* solver was utilized in the current work to perform dynamic mesh motion of a printing needle type nozzle. The laminar model was utilized in these solvers of the current study. The following equations are the underlying PDE's for laminar flows:

Continuity equation – for incompressibility constraint

$$\nabla . \boldsymbol{U} = 0 \qquad \textit{Equation 10}$$

Momentum equations – for momentum transport

$$\frac{\partial \rho \boldsymbol{U}}{\partial t} + \nabla . (\rho \boldsymbol{U}\boldsymbol{U}) = -\nabla p + \nabla . \left(\mu_{eff}[\nabla \boldsymbol{U} + (\nabla \boldsymbol{U})^T]\right) - \rho \boldsymbol{g} + \boldsymbol{F}_s \qquad \textit{Equation 11}$$

Phase continuity equation

$$\frac{\partial \alpha_l}{\partial t} + \nabla . (\alpha_l \boldsymbol{U}) = \nabla . (\alpha_l \alpha_g [\boldsymbol{U}_g - \boldsymbol{U}_l]) \qquad \textit{Equation 12}$$

Where;

$$\boldsymbol{U} = \alpha_l \boldsymbol{U}_l + \alpha_g \boldsymbol{U}_g \qquad \textit{Equation 13}$$

$$\rho = \alpha_l \rho_l + \alpha_g \rho_g \qquad \textit{Equation 14}$$

$$\mu = \alpha_l \mu_l + \alpha_g \mu_g \qquad \textit{Equation 15}$$

$$\mu_{eff} = \alpha_l \mu_{eff-l} + \alpha_g \mu_{eff-g} \qquad \textit{Equation 16}$$

$$\boldsymbol{F}_s = \sigma k(r)\boldsymbol{n} = \sigma \nabla . \boldsymbol{n} \frac{\nabla \alpha_1}{|\nabla \alpha_1|} \qquad \textit{Equation 17}$$

Where $\boldsymbol{F}$ is the surface tension force, $\boldsymbol{k}$ is the interface curvature and $\boldsymbol{\sigma}$ is the surface tension.

### 3.2.3. The Turbulence Model

The laminar nature of the flow is evident from the low Reynolds number in the modelled cases. The following equation defines the Reynolds number.

$$Re = \frac{\acute{u} d}{\nu} \qquad \textit{Equation 18}$$

Where $\bar{\boldsymbol{u}}$ is the cross sectional averaged velocity and $\boldsymbol{d}$ is the characteristic length of the flow or the hydraulic diameter of a closed channel $\left(d = {}^{4A}/_{P}\right)$, where **A** is the cross-sectional area, and **P** is the wetted perimeter. The Reynolds number for the flow in the current designs is less than a hundred. In this range, the flow should be laminar, but due to the flow behavior in the primary validation study, boundary layer separation and vortices at the sharp edges were noticed. Therefore, a suitable LES model was selected instead of the laminar model.

### 3.2.4. The One Equation Eddy Viscosity Model

The turbulence model for the mixing cases is the large eddy simulation (LES), which is the one equation eddy viscosity model (*oneEqEddy* LES model in *OpenFOAM* turbulence properties). The eddy viscosity model uses equation 19 for an effective turbulent viscosity that is turbulence dependent;

$$\mu = \mu_{eff} + \mu_{turbulent} \qquad \textit{Equation 19}$$

Where $\boldsymbol{\mu}$ is the effective turbulent viscosity, $\boldsymbol{\mu_{eff}}$ is the effective mixture viscosity, and the *Boussinesq* eddy viscosity, $\boldsymbol{\mu_{turbulent}}$, which is defined as;

$$\mu_{turbulent} = C_S^2 \rho \Delta^2 |\bar{S}| \qquad \textit{Equation 20}$$

Where $\boldsymbol{C_s}$ is a constant that is model parameter, $\boldsymbol{\Delta}$ is the filter cutoff width (the characteristic length scale of the SGS eddies), and $\boldsymbol{S}$ is the strain rate of the resolved field.

The LES model was selected over the RANS given the availability of computing resources, and the suitability for the modeled cases. RANS works by a time filter that removes the scales of motion

for time scales below the filter width (the average $\boldsymbol{u_i}$ = 0), while the filter in LES is spatially based. In LES, instead of closure relations based on the turbulent kinetic energy and the turbulent dissipation rate, the closure relation is dependent on the length scale of the computational grid. The LES models resolve all the scales except for the small eddies (below the filter width) which are modeled.

The basic LES Smagorinsky model tends to overestimate the eddy viscosity near the surface. However, the selected LES model is the one equation eddy model, a sub-grid scale model (SGS), where SGS is the spatial region below the resolved length scale. The *oneEqEddy* model represents the eddy viscosity similar to the Smagorinsky model, but uses an additional transport equation for the SGS turbulent kinetic energy $\boldsymbol{k}$, which is a model balanced turbulence kinetic energy [37] [38];

$$\frac{\partial k}{\partial t} + \nabla.(\boldsymbol{U}k) - \nabla.\left(\nu_{eff}\nabla k\right) = -2.0\nu_{eff}|\bar{S}| - {C_e k^{3/2}}/{\Delta} \qquad \textit{Equation 21}$$

Where the LHS terms are (left to right): temporal change in the SGS kinetic energy, convection of $\boldsymbol{k}$, and the diffusion of $\boldsymbol{k}$. And the RHS terms are source terms (left to right) which is defined by Eugene as "*the decay of turbulence from the resolved scales to the sub grid scales via the energy cascade*" [38], and the turbulence dissipation.

# Chapter 4. Methodology

The objective of the current study is to investigate two of the initial stages of the proposed production process. The processes are defined as the mixing of reagents and the droplet generation stages (figure 6).

The first mixing stage is defined to have controlled mixing which ensures a sufficient level of mixing. Thus, the current study investigates various designs of passive microfluidic mixers (feasible-to-make) for evaluation of their mixing efficiency and the resultant mixing time and length. CFD modelling using OpenFOAM *twoLiquidMixingFoam* solver was used for this modelling step. First, the mixing phenomena as modelled by the selected solver have to be validated by experimental values reporting the mixing efficiency of other microfluidic mixers available in literature.

Second, the droplet generation stage was investigated with the OpenFOAM solver (*interFoam* and *interDyMFoam*) to estimate the droplet generation time and the droplet size.

The equations that are used in their discretized form by the numerical solvers contain physical constants of the fluids of interest. These are the viscosity, mutual diffusivity, and others. However, such values were not available in literature. Therefore, before numerical modelling, a series of experimental measurements of the fluid properties were conducted including: rheology, and diffusivity measurements.

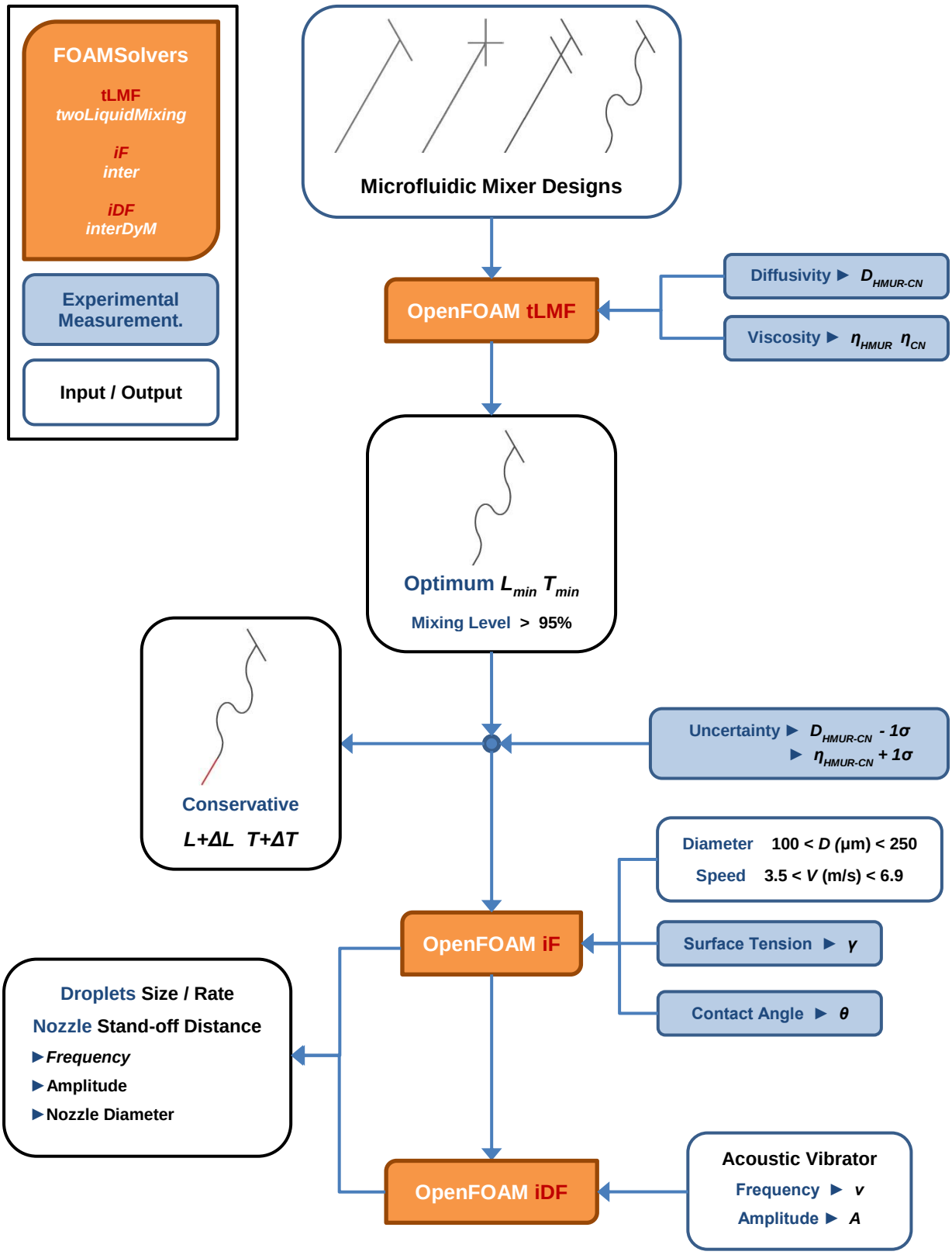


*Figure 6: A scheme of the current study.*

# Chapter 5. Experimental Measurements

Physical properties such as the viscosity, mutual diffusion coefficient, surface tension, and contact angles are required for the fluids: CAN, HMUR, and the reference 3D printing solution (1.255/1.945 CAN to HMUR). These physical properties are constants in the equations that are meant to be solved by OpenFOAM. In quantifying the MF mixing efficiencies, the molecular diffusivity coefficient is required. Also, the droplet generation process is governed by the surface properties of the fluids and the rheology. To the best of our knowledge, such physical properties of these fluids are not available in the literature. And so, experimental measurements for the rheology and diffusivity were conducted.

## 5.1. The Rheology

The rheology was performed in the laboratories of ETH Zurich (Professorship of Complex Materials). The rheometer (Modular Compact Rheometer MCR 502) of the company Anton Paar was used for this purpose. The rheometer is a rotational viscometer that evaluates the viscosity from the torque value required to achieve a certain rotational speed of an object inside the fluid. The fluid is enclosed between the fixed surface (an outer cylinder) and the variable speed, rotating cylinder (an inner cylinder). The results of such measurements at three different temperatures of the CAN and HMUR solutions versus the shear rate are shown in figures 7 and 8, respectively.

The viscosity of the mixture of the two fluids was evaluated as a linear function of the viscosity of the mixing fluids (a linear function of the concentration of each fluid) provided that no reaction has taken place. This approach was implemented in OpenFOAM (*interFoam* solver). The mixture viscosity would not be linear with the volumetric fractions as explained by Gambill [39]. However, the OpenFOAM linear model was adapted. The purpose of such interpolation was to measure the viscosity of each fluid separately to avoid the complexity of having a gelled mixture at elevated temperature which is characterized by a sharp increase in the mixture viscosity [27].

Shear thinning property is advantageous in 3D printing, which is characterized by a decrease in the viscosity at high shear rates. In a microfluidic device, large pressure gradients are expected between the inlets and outlets. Such a decrease in viscosity results in less of a pressure drop in the micromixers, and to have a more viscous fluid once the droplets are generated. After generating the droplets, a viscous fluid is advantageous to maintain the droplet shape till the online-heating comes into force.

Both solutions have nearly constant viscosities for shear rates of more than 100 $s^{-1}$ (figures 7 and 8). The importance of these shear rates is that they are encountered in the microfluidic mixer designs that are proposed in this study. Both fluids are Newtonian in this range of shear rates (no dependence on the shear rate). The average viscosity values are listed in table 1.

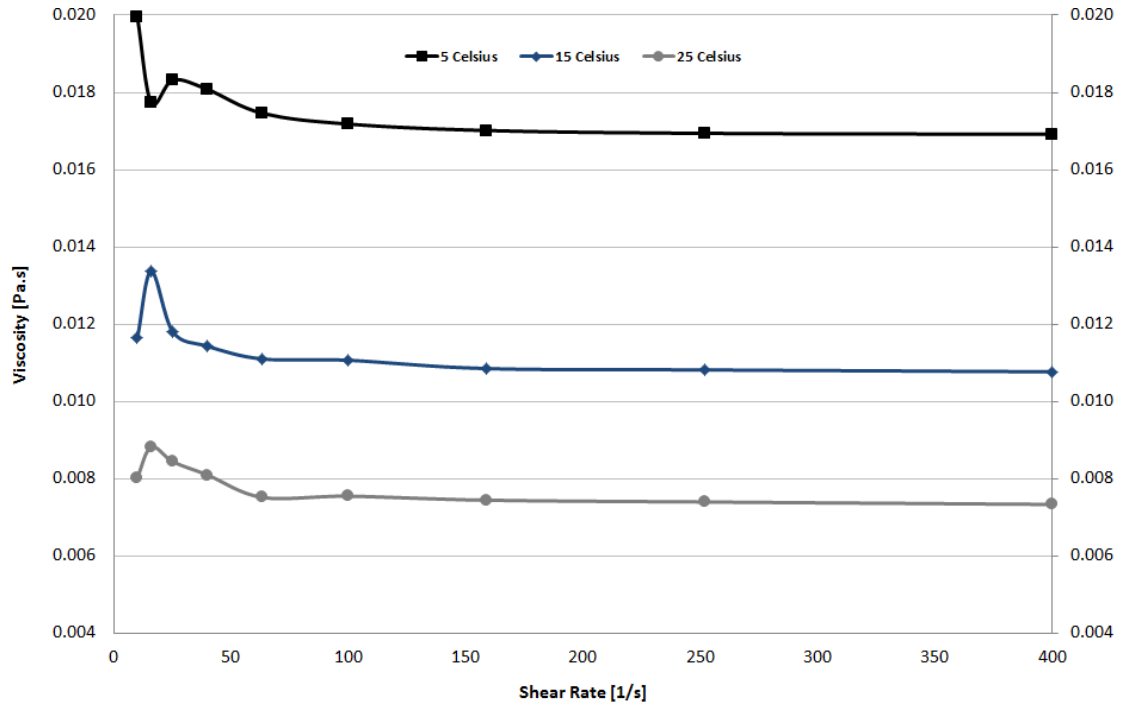


*Figure 7: The viscosity of the CAN solution vs the shear rate.*

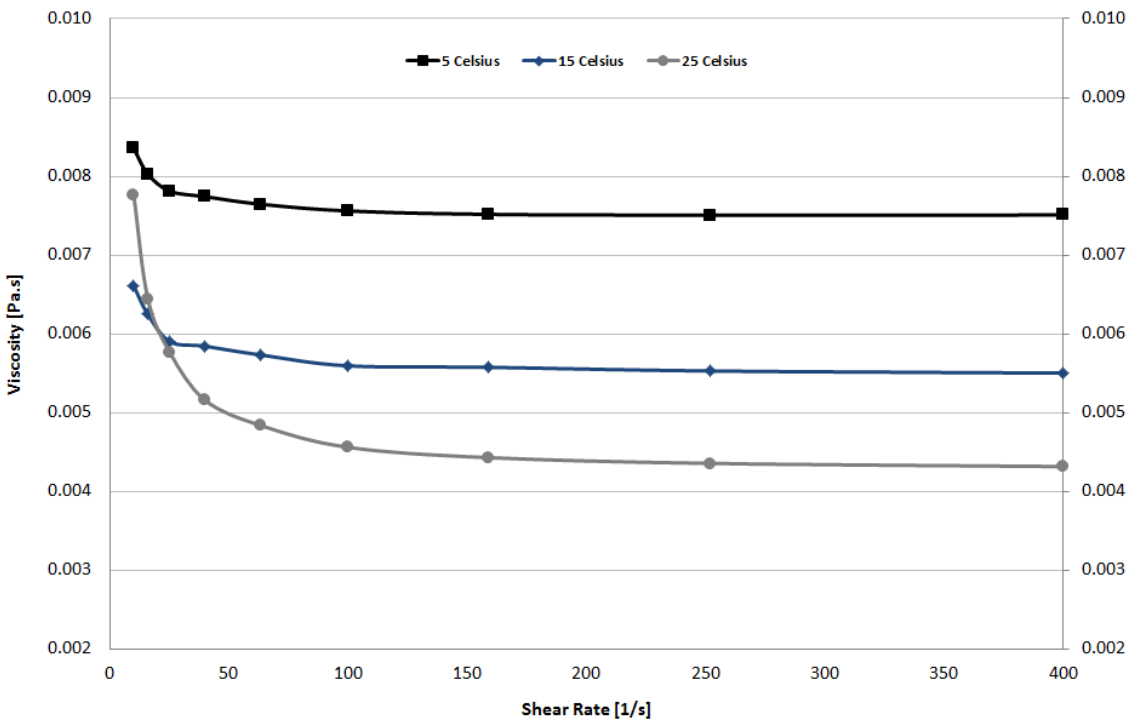


*Figure 8: The viscosity of the HMUR solution vs the shear rate.*

*Table 1: The average viscosity of the CAN, HMUR and the reference solution (x10$^{-3}$ [Pa.S]).*

| Solution | CAN | HMUR | Ref. Solution |
|---|---|---|---|
| °5 | 7.520 ± 0.021 | 16.997 ± 0.076 | 13.280 ± 0.056 |
| °15 | 5.542 ± 0.011 | 10.854 ± 0.091 | 8.771 ± 0.065 |
| °25 | 4.397 ± 0.056 | 7.412 ± 0.037 | 6.230 ± 0.048 |

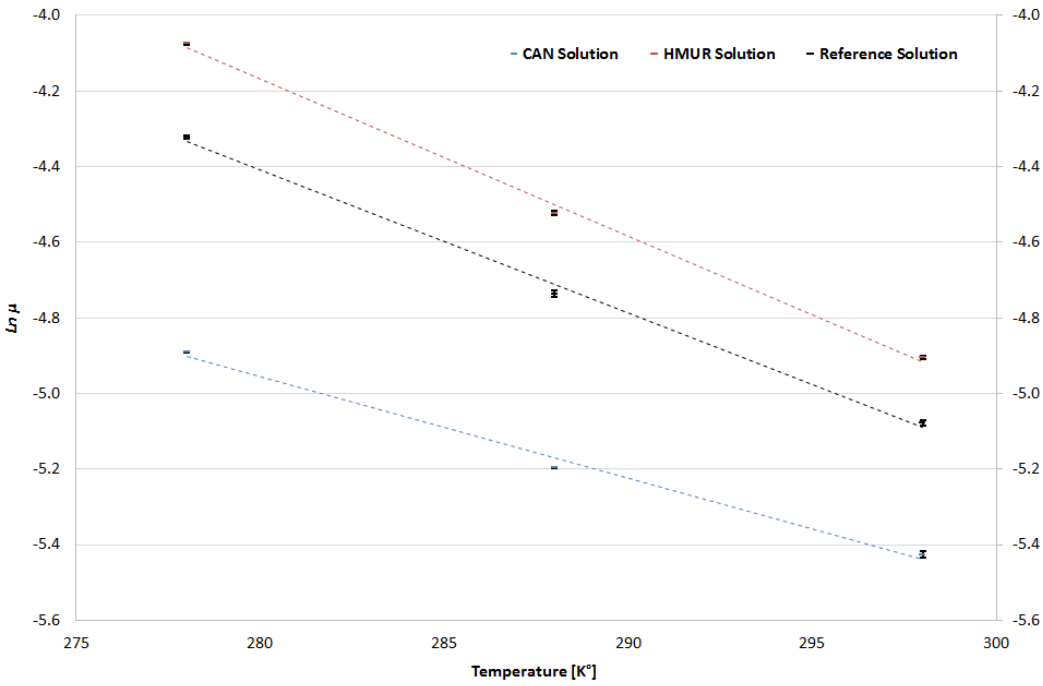


*Figure 9: The viscosity of the CAN, HMUR and the reference solutions at 5, 15, and 25 °C.*

According to the Arrhenius model, the viscosity is showing exponential dependence on the absolute temperature [40] (first order fluids or power-law fluids). The natural logarithm of the viscosities versus temperature of the two solutions is shown in figure 9. The standard deviations of the of viscosities temperature-dependency from the exponentiality function are: 0.030, 0.027 and 0.030 for the CAN, HMUR and the reference solution, respectively. The relative error is less than 1% for both fluids from the exponential dependence. The following logarithmic fitting can be used to interpolate the value of viscosity for a different value of temperature [K°]:

*The CAN solution:* $(ln\,\mu \pm 0.017) = -0.0268\,T + 2.5558$ *Equation 22*

*The HMUR solution:* $(ln\,\mu \pm 0.016) = -0.0415\,T + 7.4502$ *Equation 23*

*The Reference solution:* $(ln\,\mu \pm 0.017) = -0.0365\,T + 5.7397$ *Equation 24*

## 5.2. The Surface Tension

By generating droplets from the printing head, a liquid-gas interface forms, which has a unique energy per unit area (the surface tension). This value affects the droplets size. The surface tension was

measured in the laboratories of ETH Zurich (Institut für Verfahrenstechnik) using the tensiometer (Force Tensiometer – K11) of the company KRÜSS GmbH, using the Wilhelmy plate method.

The surface tension depends on the liquid-gas interface as well as the composition of the liquid at the interface and the gaseous volume nearby. For a binary mixture, the surface concentrations do not equal the bulk value, and so the vapor pressure is not a function of the bulk concentration, but rather its surface concentration. Usually, a binary mixture will negatively deviate from the bulk concentration based value. The lower surface tension fluid will preferentially enrich the surface to reduce the Helmholtz free energy. Hence, the surface tension of a binary mixture is not commonly interpolated based on the bulk concentration, but rather linearly in the surface layer molar fraction [41].

It was not possible to control the temperature using the available experimental setup since the mixture was not stable at low temperatures such as 10 °C. Consequently, the surface tension of the two fluids was measured separately and the maximum error was evaluated for the mixture based on the bulk concentration (figures 10 and 11). Commonly, the surface tension decreases up to the critical point as predicted by Eötvös rule [42] [43]. The CAN solution does not follow Eötvös rule, while the HMUR follows this rule. Both solutions have surface tension values close to that of pure water.

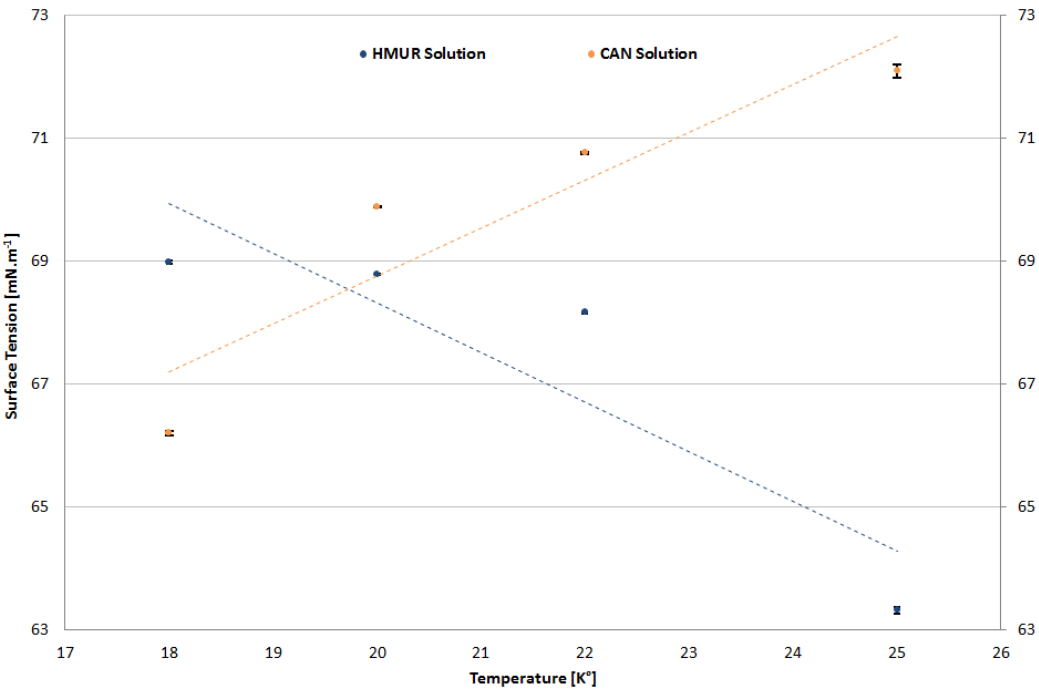


*Figure 10: The surface tension of the CAN and HMUR solutions at 18, 20, 22, and 25 °C.*

The relative errors are 0.8% at 20 °C and 2.1% at 18 °C. The closeness of the surface tension values enabled approximating the surface tension of the mixture as a linear function of the bulk concentration. It has been estimated that the error is small enough for the current study. The expected

deviations will be qualitatively less than these errors for the following factors. Firstly, the two solutions are dissolved salts in water, and their vapor pressure which is the driving force for separation is low. Secondly, the printing process is characterized by high velocities in the nozzle region and separation of the bulk and surface concentrations need sufficient time, not being effective here. The maximum error was calculated assuming that the surface layer molar fraction can be equal to the molar fraction of the bulk fluid or enriched in the low surface tension fluid.

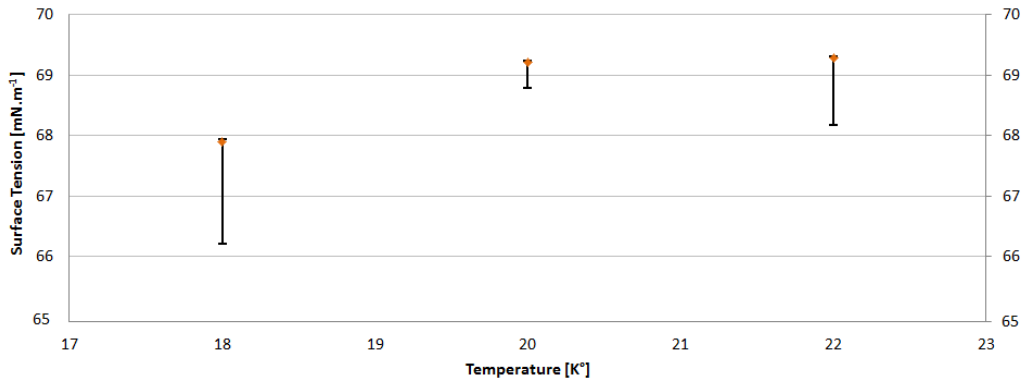


*Figure 11: The surface tension of the reference solutions at 18, 20, and 22 °C. The surface tension can be interpolated as:* $\gamma = 69.22 \pm 0.43\ [mN.m^{-1}]$ *at 20 °C.*

## 5.3. The Contact Angles

At the stage of droplet generation, a solid-liquid-gas interface is formed on the contact line between the droplet and the printing head (three phase contact line). According to Young's equation, the contact angle that is formed by the intersection of the liquid-solid and the liquid-vapor interfaces is characteristic by that three phase contact line and it is a measure of the wettability [44]. A liquid with good wettability (drophilic) will maximize the contact lines and will have a contact angle <90°. Wetting is not a static phenomenon due to surface heterogeneity (topologically or chemically), and the angle of contact will have a spectrum "dynamic contact angle" [45]. The Young equilibrium contact angle will be in-between these two values: the advancing contact angle $\boldsymbol{\theta_a}$ (maximal) and the receding contact angle $\boldsymbol{\theta_r}$ (minimal). A large difference is not favorable and should be minimized by surface preparation through inerting or smoothening the surface as much as possible. The difference between these angles is the contact angle "*Hysteresis*"; $H = \theta_a - \theta_r$.

The contact angles of the CAN and the HMUR solutions have been measured on a stainless-steel surface separately for each solution (due to mixture instability) in the laboratories of ETH Zurich (Institut für Verfahrenstechnik). The measurements are based on a telescope-goniometer (observation of the contact angle a droplet will make on a stainless-steel surface) and using the drop shape analyzer DSA25S (Krüss GmbH, Germany). The Young's equilibrium contact angles were calculated from the measured values based on Tadmor [46]. Selected images are shown in figures 12 and 13 along with the calculated static contact angles.

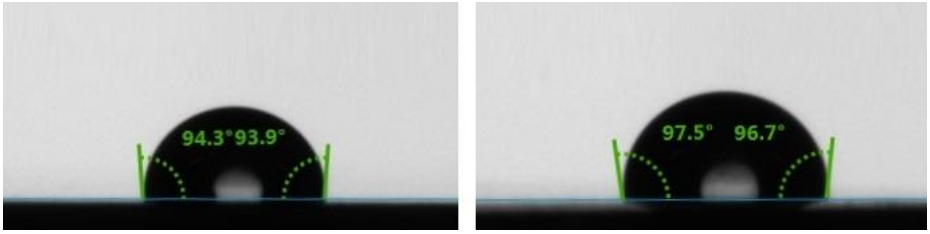


*Figure 12: Droplets of the CAN solution ($H_{CAN}$ = 97.5° - 84.5° and $\vartheta_{CAN}$ = 89.9°).*

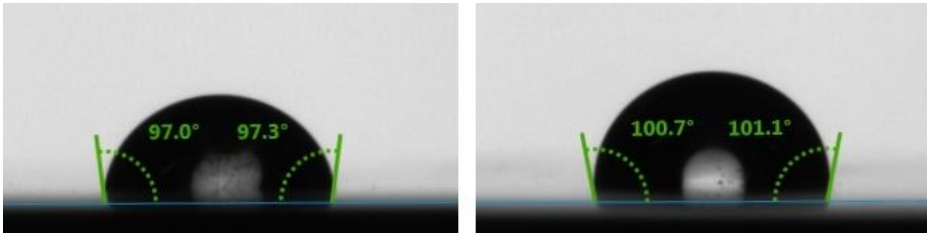


*Figure 13: Droplets of the HMUR solution ($H_{HMUR}$ = 106.7° - 87.9° and $\vartheta_{HMUR}$ = 94.4°).*

## 5.4. The Mutual Diffusivity

The mutual diffusivity is defined as the extent to which one specie will diffuse into another, and so, it is a physical property of both the CAN and HMUR solutions, which is not reported in literature to our knowledge. The mutual diffusivity between the CAN and HMUR solutions was evaluated as a function of temperature to extrapolate the evaluated coefficient to the production temperature. The mutual diffusion coefficient typically shows linear temperature dependence as expected from Stokes-Einstein equation [47]. Diffusivity is a Fickian process, where the driving force is the concentration gradient without convective currents that results in equal counter flows that flatten this gradient. The phenomena is described using Fick's first law of diffusion [12] (equation 1). Typical approaches to measure the mutual diffusion coefficient are: molecular dynamics [48]; empirically from the self-diffusion coefficients; and experimentally [49] [50] [51]. The experimental approach based on Taylor dispersion analysis is explored in the current study.

### 5.4.1. The Theory of Taylor Dispersion Analysis

A common experimental approach to evaluate the mutual diffusivity is the Taylor dispersion analysis (TDA) [49] [50] that was proposed by Taylor [51] and later detailed by Aris [52] and Alizadeh et. al [49]. The TDA is based on the dispersion of a small amount of a solute that is injected into a capillary where a second carrier fluid is flowing. The second solution carries the injected solute along the capillary and the solute dispersion is caused by the molecular diffusivity and the convection. Later, the solute pulse develops into a Gaussian distribution (figure 14). Monitoring a selected physical property of one solution will reveal the extent of diffusivity. And as explained in the original theory, the Gaussian shape is only reproducible for a physical property that is linearly correlated to the concentration.

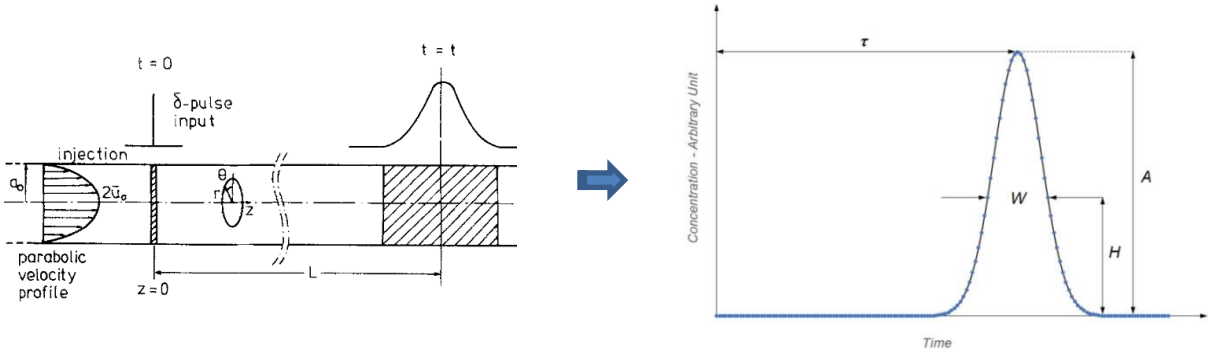


*Figure 14: A TDA data downstream of an injection point, after τ from the injection time [48].*

The temporal variance of the Gaussian distribution, as represented by the first two temporal moments will depend on both the average flow velocity and the molecular diffusivity. Various empirical models are used for this purpose. The theory behind this approach and the basis of operation of an instrument on this principle are explained by Alizadeh et. al [49]. The fitting parameters are:

***1- <u>The Temporal moments (mean time and variance)</u>***

The fitting parameters are the first two temporal moments: $\boldsymbol{\tau}$ (the mean or the retention time) and $\boldsymbol{\sigma}$ (the variance) of the Gaussian distribution. According to Alizadeh et. al [49] [50] and Ghanavati [53]:

$$C(t) = A_0 + Ae^{[-(t-\tau)^2/2\sigma^2]} \qquad \textit{Equation 25}$$

where $\boldsymbol{A}$ is the peak height. Two constants can be evaluated; the mutual diffusivity $\boldsymbol{D}$, and the dispersion coefficient $\boldsymbol{K}$. According to Erkey et al. [54], the mutual diffusivity can be evaluated as:

$$D = \frac{R^2\tau}{24\sigma_t^2} \qquad \textit{Equation 26}$$

The dispersion coefficient relates to the mutual diffusivity $\boldsymbol{D}$ according to the equation of Aris [55];

$$K = D + \frac{R^2v^2}{48D} \qquad \textit{Equation 27}$$

Where $\boldsymbol{R}$ is the capillary internal radius and $\boldsymbol{v}$ is the mean carrier velocity.

***2- <u>The peak widths (W) and the fractional heights (h)</u>***

The width-height approach is used in literature where there is more than one diffusing molecule and the Gaussian distribution is not reproduced. The peak widths $\boldsymbol{W}$ at fractional heights $\boldsymbol{h}$ are used to evaluate the multi-diffusivity between the two solutions, and according to Callendar and Leaist [56].

$$D_h = -\frac{\ln h}{3}\frac{R^2t_R}{W_h^2} \qquad \textit{Equation 28}$$

Both empirical approaches are used to in the current study, along with a comparison between their results. This approach is used to study the polydisperse diffusivity of the urea and HEXA mixture. The mixture is composed of five species (table 4) and the diffusivity is polydisperse that depends on the mass of the molecules, molecular size, and other factors. Additionally, the first empirical model

was modified in the current study to account for this polydisperse diffusivity by linearly superimposing Gaussian fits.

The advantages of the TDA compared to other approaches are the reliability of the results and the accuracy, uncertainties of ~1% is typical. Also, TDA is performed in a short run time with straightforward setup and a valid theory and equations. Temperature and the molarity dependency can be evaluated also [53] [57] [58]. For a successful TDA, several parameters were controlled:

- The temperature and molarity of both fluids were fixed
- A microfluidic capillary was used (only Fickian diffusivity without convective transport)
- The solute volume was small (infinite dilution)
- The flow rate was accurately monitored (HPLC is used to accurately evaluate the retention time)

### 5.4.2. The Apparatus

The TDA was performed at the University of Fribourg, Adolphe Merkle Institute, using the UV area imaging detector ActiPix D100 of the Paraytec company. The detection is based on the ultra-violet (UV) absorbance of the fluid, that is detected by a 'self-referencing' active pixel sensor array [59].

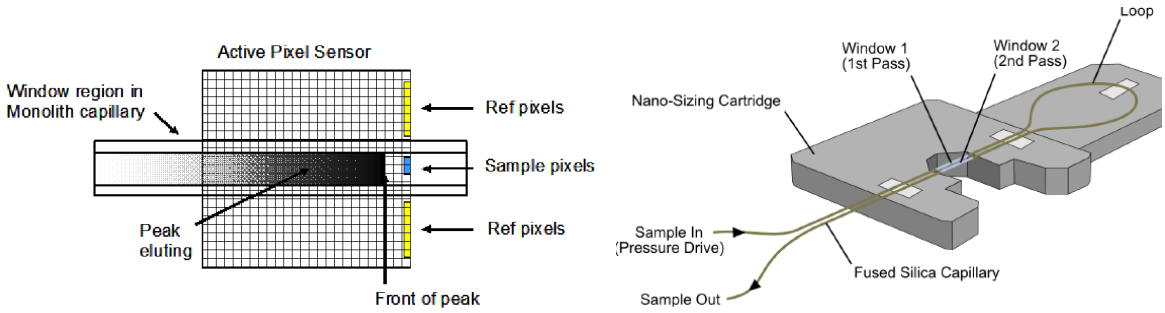


*Figure 15: The self-referencing detector (left) and the multi-pass capability of (right) of the TDA [58].*

The UV detector measures the absorbance ***A*** of a specific wavelength of the transmitted light. To calibrate the detector to a wave length, which is absorbed by one of the fluids, spectral absorbance measurement was performed using an absorption spectrometer. The characteristic wave length of the CAN solution is 488 nm. A 12 nL solute volume is pumped through a multi-port valve into the capillary, where the pump drives the carrier solution up to the ActiPix D100 detector. The column is coiled so that multiple sections of the capillary will be analyzed. The experimental parameters are listed in table 2, along with the weight and molar fractions of both solutions in table 3 and 4.

*Table 2: The TDA parameters for the three temperature measurements.*

| | | | |
|---|---|---|---|
| Injection volume (nL) | 12.24 ±0.01 | Capillary internal Diameter (μm) | 76 ±1 |
| Flow velocity (mm/s) | 0.6276 ±0.0001 | Retention Length (First Window) (cm) | 66.4 ±0.1 |

*Table 3: The density and the volume fractions of the two mixing solutions.*

| Solution | Abbreviation | Density (g/cm) | Vol% |
|---|---|---|---|
| Methenamine + Urea | HMUR | 1.142 | 60.8 |
| Cerium Ammonium Nitrate | CAN | 1.500 | 39.2 |

*Table 4: The weight (top) and molar fraction (bottom) of the CAN and HMUR solutions.*

| Solution | $H_2O$ | NaOH | $Ce(NO_3)_6(NH_4)_2$ | $(CH2)_6N_4$ | $CO(NH_2)_2$ |
|---|---|---|---|---|---|
| Cerium Ammonium Nitrate | 44.2% | - | 54.8% | - | - |
| Methenamine + Urea | 41.2% | 4.0% | - | 39.2% | 16.8% |
| **Solution** | **$H_2O$** | **NaOH** | **$Ce(NO_3)_6(NH_4)_2$** | **$(CH2)_6N_4$** | **$CO(NH_2)_2$** |
| Cerium Ammonium Nitrate | 96.1% | - | 3.9% | - | - |
| Methenamine + Urea | 77.6% | 3.4% | - | 9.5% | 9.5% |

### 5.4.3. The TDA Results

The flow rate is so low that secondary flows are negligible, which is a criteria that is established by Taylor in driving the empirical equations from Fick's law. The Reynold numbers are between 0.010 and 0.013. An additional criteria that is necessary for the solute pulse to develop into a Gaussian distribution is the Levenspiel-Smith criterion ($D/_{vL} < 0.01$), which is related to the reciprocal of the Péclet number [57] [60]. In the current experiment: $2.1x10^{-05} < D/_{vL} < 7.6x10^{-05}$ , and the criteria was met.

The two solutions have five components with different molar fractions. Once a fluid is injected into the other, the five species will diffuse to flatten the concentration gradients. The rates depend on the diffusivity of each specie and the concentration gradients. The water diffusivity was neglected in the data analysis, since the gradient is ~6.7%, the driving force for the diffusion is low. Also, the NaOH diffusivity was neglected in the analysis of the TDA data. The mutually diffusing species are the three components: urea, HEXA and cerium ammonium nitrates. The first two are in the HMUR solution (solute) and the latter is in the CAN solutions (carrier). Since the mutual diffusivity is a unique value between two species, two mutual diffusion coefficients resulted from the data analysis, one for the urea into the CAN and the other for the HEXA into the CAN solution. The approximation of fitting the TDA data to only two diffusing species yielded satisfactory results.

***1- <u>Fitting the temporal moments (mean time and variance)</u>***

Since the diffusivity is polydisperse between the two solutions, the TDA experimental setup was modified so that the HMUR will disperse in the CAN solution. Also, instead of measuring the absorption index of the solute, the setup is to measure the absorption index of the background, the CAN solution. By arranging the setup in this configuration, the absorption index measurements are

related to the dilution of the background. And since the HMUR has two main diffusing species, there will be two superimposed dilution patterns in the TDA data, which are related to two species diffusing from the solute pulse (the urea and the HEXA). Under this experimental setup, the TDA data could be fitted to two linearly superimposed Gaussians distributions representing two diffusing species, by minimizing the squared differences of the TDA from the following fitting equation:

$$I(t) = A_0 + A_1 e^{[-(t-\tau_1)^2/2\sigma_1^2]} + A_2 e^{[-(t-\tau_2)^2/2\sigma_2^2]} \qquad \textit{Equation 29}$$

Four fitting variables (the temporal moments $\boldsymbol{\tau_i}$ and $\boldsymbol{\sigma_i}$) was then used to evaluate two diffusion coefficients:

$$D_i = \frac{R^2 \tau_i}{24\sigma_i^2} \qquad \textit{Equation 30}$$

The evaluated diffusivities are listed in table 5. The experimental errors of the coefficients were evaluated from the standard deviation of the two temporal moments and the systematic errors, which are acceptable for the scope of the current study. The experimental error is higher than the values reported in literature, since the current approach was to fit two Gaussians instead of one. The fitted curve along with the TDA data are shown in figures 16 and 17. The first figure is the TDA at 8 °C and the latter is the TDA at 16 °C. At 16 °C, the middle part of the data was excluded in curve fitting, since these changes in the AI relate to the gelation. The gelled volume lags in the TDA, and blockage of the capillaries was even encountered. The two Gaussians can be reconstructed from the left and right parts of the data but with larger bounds, since the number of fitting parameters is 7 and the degree of freedom is more than a thousand.

### *2- <u>Fitting the peak widths and fractional heights</u>*

The widths of the TDA data were evaluated at several heights. Two techniques were used to invert the TDA data, by curve fitting the data to four polynomials, and by sampling the TDA data at a specific height interval. The diffusivity results from the first technique are shown in table 6 and were evaluated using equation 30, along with the deviation from the former Gaussian technique. No data exclusion was done in the second approach, which explains the large standard deviations for the width-height approach. The results of both approaches are shown in figures 18 and 19.

The methenamine molecule, which is ~2.3 times heavier than the urea molecule, will mostly be the low diffusing species. And so, figures 18 and 19 are split into two sections of two different diffusivities, where the left is for the methenamine and the right is for the urea molecule. The figures show the diffusivities from the Gaussians approach along with $\boldsymbol{\pm 1\sigma}$. For the width-height approach, the curve fitting along with the sampled width-height data (approx. 12 points in each section) are represented.

The two approaches resulted in acceptable accuracies for the methenamine at the two temperatures of measurements. The methenamine also tends to diffuse less and reside in the middle of the dispersed pulse. For the urea molecules, only the diffusivities at 8 °C can be relied on, since the results at 16 °C are spread along large values due to the gelation occurring during the experiments. Where the two approaches are valid, both are consistent with acceptable standard deviations. Another measure of the data consistency is the Einstein-Smoluchowski relation within the context of the kinetic theory. A form of the relation is Einstein-Stoke equation for the diffusion of spherical particles in a liquid with a low Reynolds number [61]:

$$D = {}^{T}/_{6\pi r\mu} \qquad \textit{and so,} \qquad {}^{D\mu}/_{T} = {}^{1}/_{6\pi r} = constant \qquad \textit{Equation 31}$$

Where ***r*** is the equivalent hydrodynamic radii of the diffusing molecule.

The diffusivity at a specific temperature can be used to evaluate the diffusivities at other temperatures. In the current study, it is used to check the consistency of the results using the evaluated viscosities (section 5.1). As shown in tables 7 and 8, both approaches, the Gaussians fitting and the width-height yielded large deviations between the 8 and 16 °C measurements, mainly due to the gelation at 16 °C, which suggests the unreliability of the values at 16 °C.

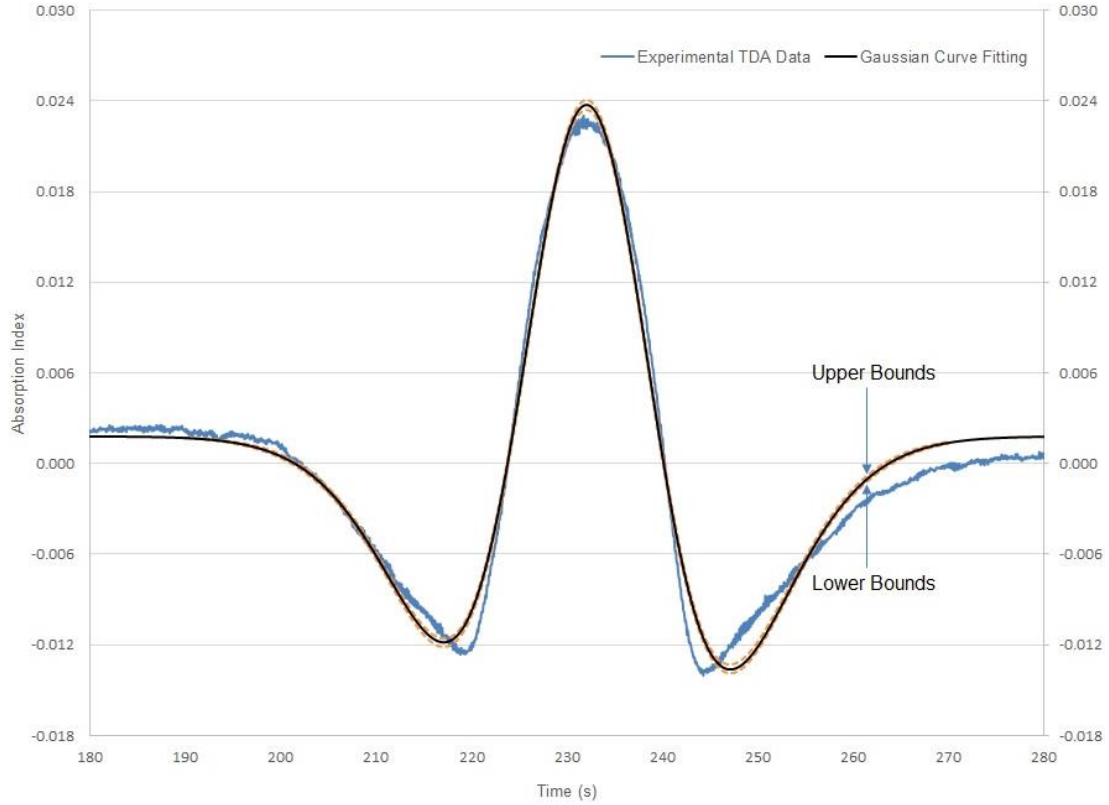


*Figure 16: TDA of the HMUR into CAN at 8 °C along with functional bounds.*

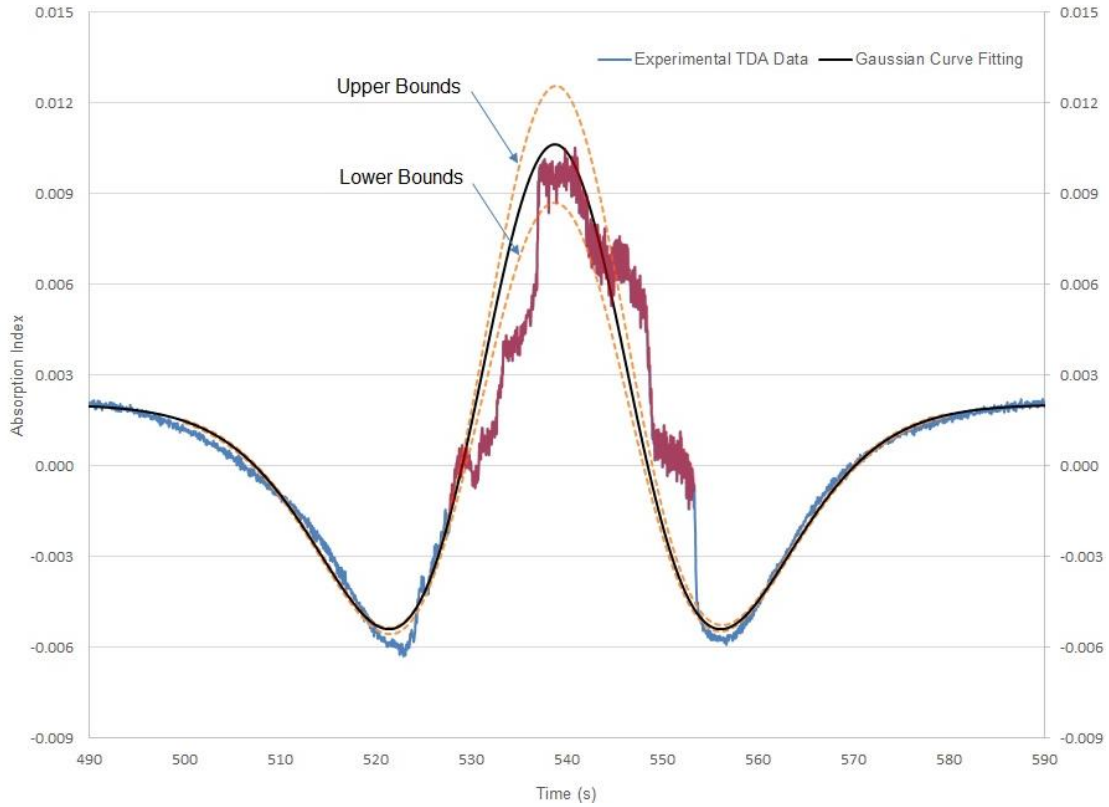


*Figure 17: TDA of the HMUR into CN at 16 °C along with functional bounds.*

*Table 5: The diffusivities of methenamine and urea into the cerium ammonium nitrate at 8 and 16 °C - superposition of Gaussians distributions.*

| Diffusing Molecule | Mutual Diffusivity x10$^{-10}$ [m$^2$/s] (into Cerium Ammonium Nitrate) | | | |
|---|---|---|---|---|
| | 8 °C | Δ$ | 16 °C | Δ$ |
| **Methenamine** | 3.787 ± 0.065 | 1.7% | 6.698 ± 0.297 | 4.4% |
| **Urea** | 10.96 ± 0.17 | 1.5% | 17.29 ± 1.03 | 6.0% |

*Table 6: The diffusivities of methenamine and urea into the cerium ammonium nitrate at 8 and 16 °C - correlating the width of the distribution to the fractional height.*

| Diffusing Molecule | Mutual Diffusivity x10$^{-10}$ [m$^2$/s] (into Cerium Ammonium Nitrate) | | | | | |
|---|---|---|---|---|---|---|
| | 8 °C | Δ*/** ($G_2$/$W_H$) -1 | *n (σ)*+ | 16 °C | Δ*/** ($G_2$/$W_H$) -1 | *n (σ)*+ |
| **Methenamine** | 4.61 ± 1.24 | -17.9% | 0.67 | 6.86 ± 0.77 | -2.4% | 0.22 |
| **Urea** | 9.13 ± 0.63 | 20.0% | 2.92 | 15.8 ± 6.1 | 9.7% | 0.25 |

*Table 7: The Einstein-Stokes's equation for the diffusivities - superposition of Gaussians.*

| Temperature | Einstein–Smoluchowski relation ( $D\mu/T = 1/6\pi r$ ) [J/(m.K)] x10$^{-14}$ | |
|---|---|---|
| | Methenamine | Urea |
| **8 °C** | 2.694 ± 0.044 | 0.9312 ± 0.0167 |
| **16 °C** | 3.34 ± 0.20 | 1.29 ± 0.06 |
| Δ Deviation - from 8 °C# | +23.8% | +38.8% |

*Table 8: The Einstein-Stokes's equation for the diffusivities - correlating the width of the distribution to the fractional height.*

| Temperature | Einstein–Smoluchowski relation ( $D\mu/T = 1/6\pi r$ ) [J/(m.K)] x10$^{-14}$ | |
|---|---|---|
| | Methenamine | Urea |
| **8 °C** | 2.245 ± 0.155 | 1.134 ± 0.305 |
| **16 °C** | 3.04 ± 1.17 | 1.32 ± 0.15 |
| Δ Deviation - from 8 °C# | +35.4% | +16.8% |

** $G_2$ – Gaussians superposition approach*
*** $W_H$ – Width-height approach*
*$ – relative experimental error*
*+ – number of standard deviations of the Gaussians evaluated diffusivities*
*# – Δ = ($D_8$ – $D_{16}$)/$D_8$*

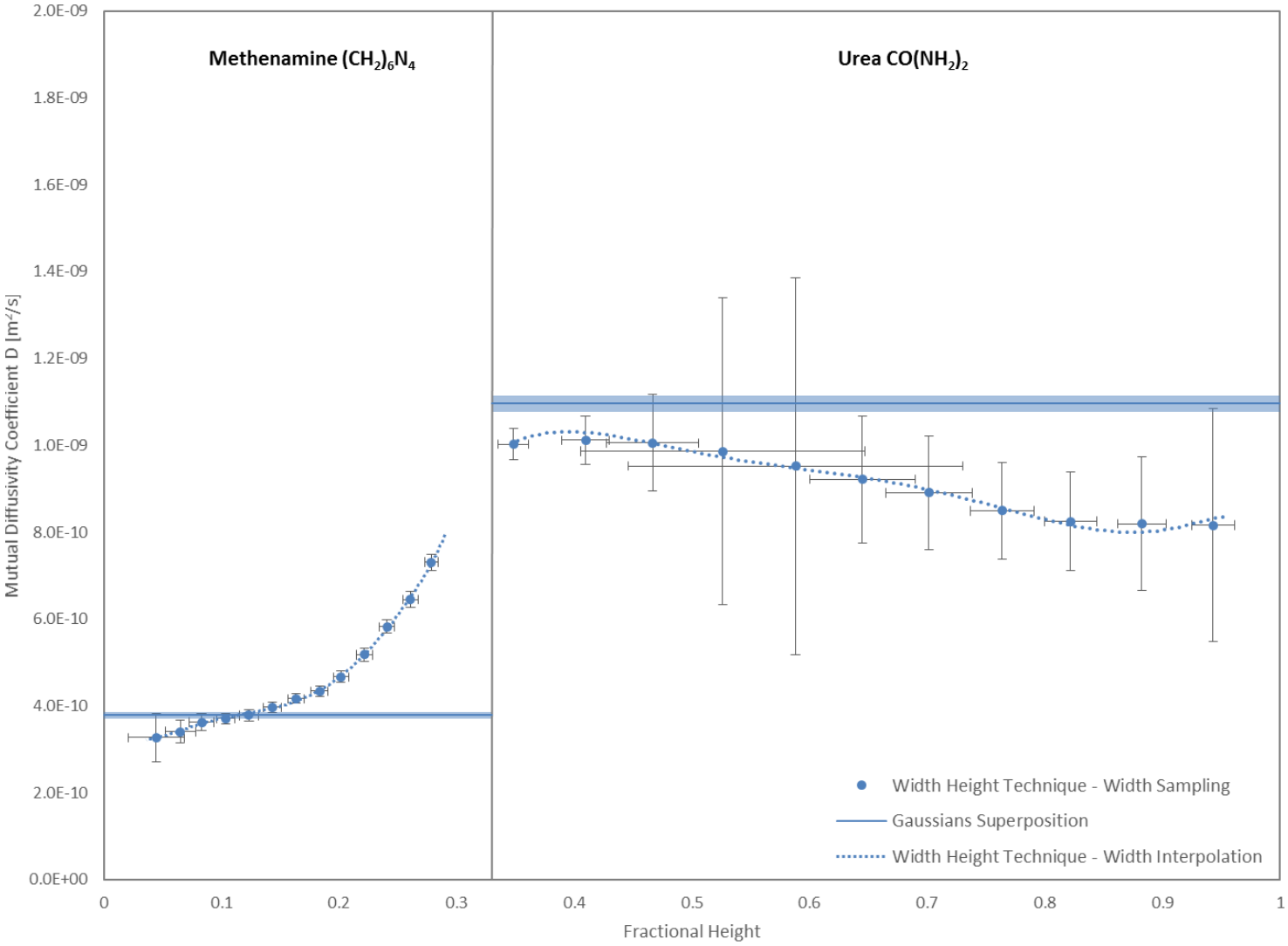


*Figure 18: The diffusivity of methenamine and urea into the CAN solution at 8 °C. Two empirical approaches are shown. The Gaussians superposition (±1σ) and the width-height technique.*

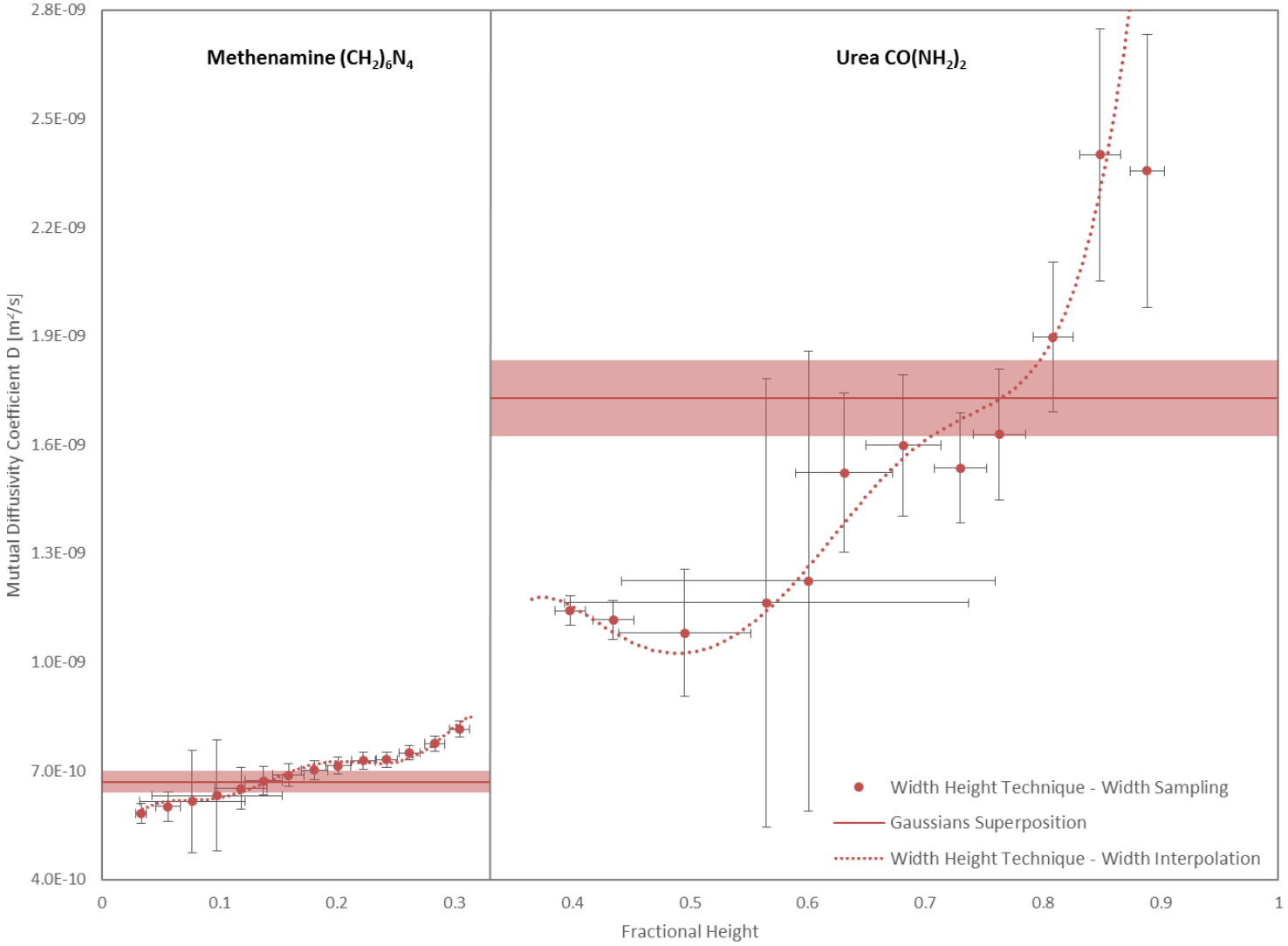


*Figure 19: The diffusivity of methenamine and urea into the CAN solution at 16 °C. Two empirical approaches are shown. The Gaussians superposition (±1σ) and the width-height technique.*

# Chapter 6. Modelling of the Mixing Phenomenon

The current study simulates the mixing in microfluidic mixers. In the simulations, several phenomena such as the effect of temperatures and surface roughness need to be isolated. Physical phenomenon, such as mixing of miscible fluids, can be modelled using numerical tools that implement the mathematical models that represent the underlying physics. A computer code solves these equations yielding variables that can be assessed experimentally or reproduced by other simulation tools. The assessment of the numerical modelling is broken down into two steps; validation and verification. Both follow different approaches and answer different questions. The former is to check the degree of which the mathematical models represent the reality, i.e., checking if the correct equations are being solved. Verification is the process of checking if the program and the computational model represent the mathematical models of the phenomenon, i.e., checking if the equations are being solved and coded in a correct way.

Validation is done through comparison with experiments, while verification is done through comparison with analytical solutions or with numerical tools solving the same set of equations. In verification, the equations are not checked for exactness with the physical phenomena, rather, they are checked if they are being solved correctly. The analytical solution is not feasible in the current study due to the complexity of the cases under consideration and the difficulty of decoupling the various phenomena. Therefore, code-to-code comparison was done with FLUENT results from the literature.

## 6.1. The Validation and Verification Case Studies

Selection of the proper case study for the validation and verification is a crucial step, because the case study must address the same phenomena, and depict as much as possible of the modelling case.

In the current study, the previous experimental and numerical simulations of Wong et al. [10] on microfluidic mixers are used for the verification and validation. Wong et al. characterized the mixing performance of microfluidic T-mixers by observing the mixing channel with an optical microscope. Additionally, simulations were performed with Fluent 6 to study the mixing phenomena [10]. The experimental results are used for the validation and the Fluent results are used to verify the OpenFAOM *twoLiquidMixingFoam* solver. The case study was selected for the proximity of the dimensions and the fluid characteristics to the micromixers under investigation. The hydraulic diameter was 55-116 micrometer and the Reynolds number ranged from 400-500.

Wong et al. [10] observed that the mixing times at the exit of the micromixers are an order of magnitude greater than what is expected by the Fickian diffusivity [62]. It is argued that mixing is not only caused by diffusion, but also through convection. The arguments are based on Fluent results resolving the flow at the mixing region of the micromixers. The simulated flow is laminar, but vortices were observed and boundary layer separation and secondary flow patterns also occurred [10].

Microfluidics are typically in the laminar regime; however, two other regimes are reported in the literature by Kockmann et al. [63]. These two regimes include vortex flow and engulfment flow, in which the fluid from one inlet engulf the other fluid beyond their intersection at high flow rates. The enhancement of the mixing characteristic was confirmed by simulations performed by Hoffmann et al. [64] in the three flow regimes recognized by Kockmann et al. [63].

### 6.1.1. The Specification of the Verification Models

The current OpenFOAM models were performed with laminar turbulence properties, similar to the reference case of Wong et al. [10] for water at 20 C°. The geometry is a simple "T" micromixer with a rectangular cross-section. The models are specified in table 10, and the reference model is case I. Case II has inlet velocities with z-component to introduce a swirling effect. Case III has different inlet velocities. Case IV has the same inlet velocities but the left inlet has twice the normal viscosity.

*Table 9: The dimensions and flow characteristics in the validation case studies [10].*

| Micro T-mixer | Geometry C |
|---|---|
| Mixing channel Width/Depth/Hydraulic Diameter [μm] | 100/51/67 |
| Applied pressure [bar] | 5.5 |

*Table 10: The velocities of the verification models [10], and the results of the OpenFOAM simulations (right column).*

| Case | Velocity - left inlet (m/s) | | Velocity - right inlet (m/s) | | NMI |
|---|---|---|---|---|---|
| | x-axis | z-axis | x-axis | z-axis | |
| I | 7.37 | 0 | -7.37 | 0 | NA – Transient Flow |
| II | 7.37 | 0.0737 | -7.37 | -0.0737 | NA – Transient Flow |
| III | 7.60 | 0 | -7.14 | 0 | NA – Transient Flow |
| IV | 7.37 | 0 | -7.37 | 0 | NA – Transient Flow |

### 6.1.2. The Results of the Verification Models

The results of all the verification models are transient, and so, the steady state mixing level of the two fluids downstream the mixing point cannot be evaluated and compared to the reported values. It is observed that vortices and asymmetric flows are developed, as shown in figure 20. Such asymmetric velocities are developed into vortices downstream of the micromixer. Such results are in contradiction to the reference work of Wong et al. [10], in which mixing level are reported for similar models.

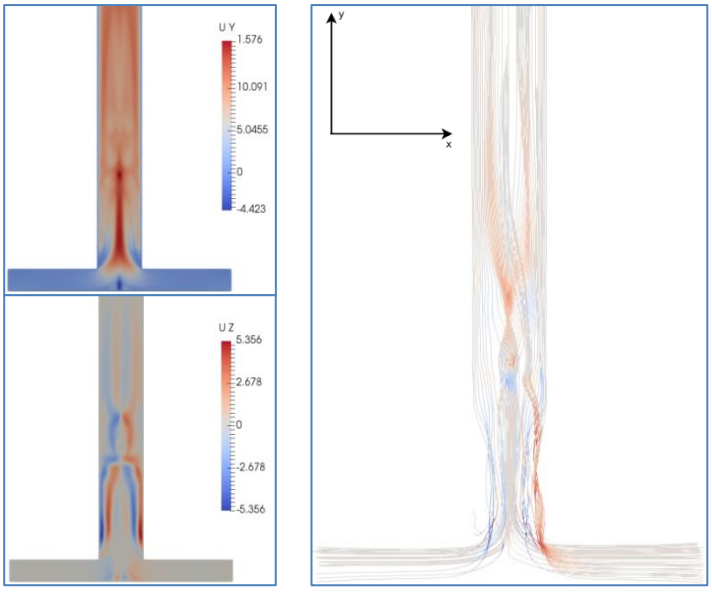


*Figure 20: The results of model II. The Y and Z velocity fields (Left), and a mid-section tracer (on vortices).*

### 6.1.3. Assessment of the Verification Models

Based on the previous discussion, the cases under-study are far from laminar. Also, the models are transient, which is expected from such asymmetric field values. These results are in contradiction to the reference publication of Wong et al. [10]. Such observation motivated the use of the LES turbulence model for the upcoming cases.

### 6.1.4. Specification of the Validation Model of Microfluidic Mixing

This section addresses a comparison between OpenFOAM results and experimental values of mixing levels of a micromixer. The motivation is that, as discussed in section 6.13, there is a large discrepancy between the OpenFOAM results and the Fluent reported results [10]. The selected case was the experimental measurements of Wong et al. [10], which are optical microscope measurements of the luminosity level across the channel depth. Complete mixing of water at 21.5 °C was considered to be achieved if the luminance deviation curve was within 95% of the mean reference level. The geometry was similar to the previous geometry in the validation section, with the exception that the mixing efficiency being evaluated 5.65 mm.

The current models are dominated by convective transport rather than diffusive transport. The local Péclet number is greater than a thousand, which is defined as:

$$Pe = Re\,.Sc = {}^{Lu}/_{\alpha} \qquad \textit{Equation 32}$$

Where ***Sc*** is Schmidt number, ***L*** is the local mesh length, and ***α*** is the diffusivity coefficient.

### 6.1.5. The Results of the Validation Models

A validation model was selected which corresponds to geometry “C” in the reference publication of Wong et al. [10]. The model was run in OpenFOAM until steady state conditions are achieved.

This was done by monitoring the convergence of the residuals and the fraction of species downstream the mixing channel into steady state constant values. The result of the validation case shows the mixing length at which a 95% mixing efficiency is achieved. These results are compared to 5.65 mm as experimentally reported by Wong et al. [10]. The OpenFOAM model underestimated the mixing efficiency compared to the experimentally reported value, where the current models resulted in a mixing level of 69%. The fraction of species (the current OpenFOAM result) is shown in figure 21 (left), which corresponds to the resulted 69% mixing level.

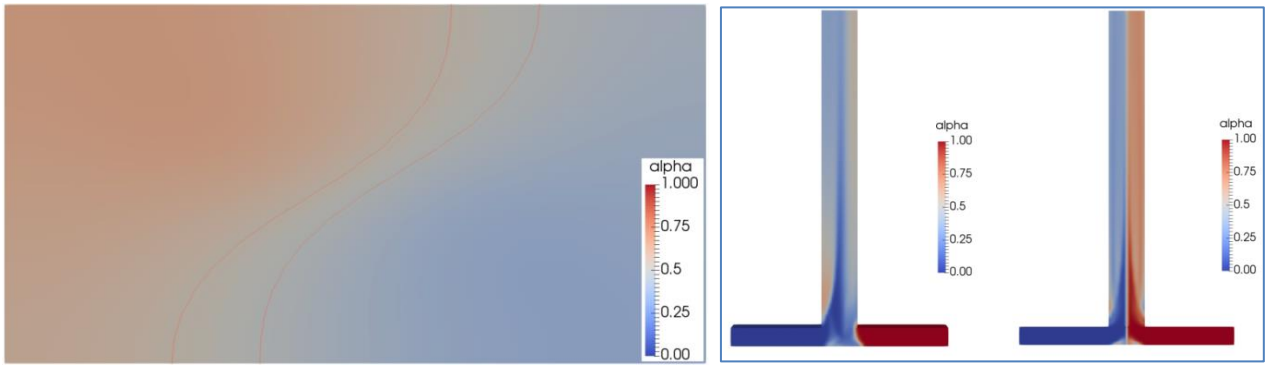


*Figure 21: The OpenFOAM results of the validation case. The fraction of species is shown at 5.65 mm from the mixing point, along with the 95% mixing criteria (left). The right horizontal plots correspond to the fraction of species at a mid-section cut (right) and the outside walls (left).*

### 6.1.6. Assessment of the Validation Models

Wong et al. [10] argued that the enhanced mixing of the micromixers is due to the vortices and the observed boundary layer separation. While the current models resulted in lower mixing values when compared to the experimental measurements, the following explanations should hold:

1- The current model implemented the correct physics, which include refinement to the boundary layers to resolve the velocity field near the walls, which resulted in an average y+ value less than unity – the viscous wall layer is well resolved.
2- The experimentally reported mixing level is an order of magnitude larger than what should be from Fickian diffusivity. The observed turbulence was not enough to result in a large mixing level.
3- It can be seen from photographs of the mixers of the experiments of Wong et al. [10], that the flow channels are not perfectly smooth. A repeated pattern is seen in all pictures, which could be an inherit surface roughness. Such heterogeneity would amplify the mixing by striation and more enhanced advection, and such irregularity is not implemented in the CFD model.

The current results are in line with previous results of Mengeaud et al. [65] and Yi and Bau [66] in which they suggested that the secondary flow around bends and sharp corners cannot alone account for the enhanced mixing in microfluidics. Therefore, it is assumed that the current models implement the correct physical models explaining the deviation from the experimentally reported values.

## 6.2. 2D Modelling of the Microfluidic Mixers (Geometry Selection)

The first aim of the current study was to select a microfluidic geometry with high mixing efficiency, i.e., the geometry that would achieve a high NMI in a short mixing length. For this purpose, several 2D models corresponding to different geometries of microfluidic mixers were modelled using the *twoLiquidMixingFoam* solver of OpenFOAM. The choice of the 2D modelling approach was to reduce the computational requirements. The NMI and the mixing times from the 2D models must not be interpreted quantitatively for a given microfluidic mixer, rather, they will be used to compare between designs. Once a geometry was justified to yield a high NMI, it was transformed into a 3D model to accurately evaluate the NMI and the mixing time. The assumptions of the 2D models are:

I. The NMIs in the 2D models were representative of the 3D models. A design that is most efficient as a 2D model will be also the most efficient design. In section 6.1, it was seen that the flow has a 3D nature. It is assumed that this 3D nature will enhance all geometries in relative proportions while the relative efficiency in the 2D modelling will be still representative in 3D modelling.
II. The geometrical effects are additive. If two features will enhance the NMI separately, a geometry that incorporates both will be more efficient than a geometry that incorporates only one feature.
III. The flow rate for each mixing fluid and the channel diameter would not change the relative enhancement in the NMI between different geometries. From this assumption, the current 2D models only use a single mixing channel width of 250 μm and a flow rate of 7.37 m/s for the HMUR solution. The CAN solution flow rate will be volumetrically adjusted.
IV. Even the flow field was represented by an LES model in the 3D models. The 2D models were performed on a laminar flow, since the LES is not intended for 2D meshes.

Mixing of the two fluids is driven by both diffusion and convection. To enhance the diffusion, multiple staggered inlets were used to increase the number of interfaces. To enhance the convection, a sharp corner in the flow channel was implemented through inlets with variable inlet angles to induce a boundary layer separation and enhanced mixing. Additionally, repetitive curvatures downstream the mixing channel were tested (figures 22 and 23).

OpenFOAM uses finite volume numerics, and therefore it requires a 3D mesh of polyhedral cells. In 2D problems, the grid was defined one cell thickness; hence, the field values are constant along the thickness axis (the z-axis). The ***+z*** and ***–z*** faces are *symmetrical* boundaries in OpenFOAM. The current cases were run until the field values converged.

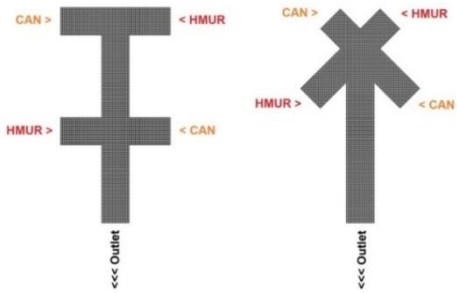


*Figure 22: The double-T and double-wedge inlets.*

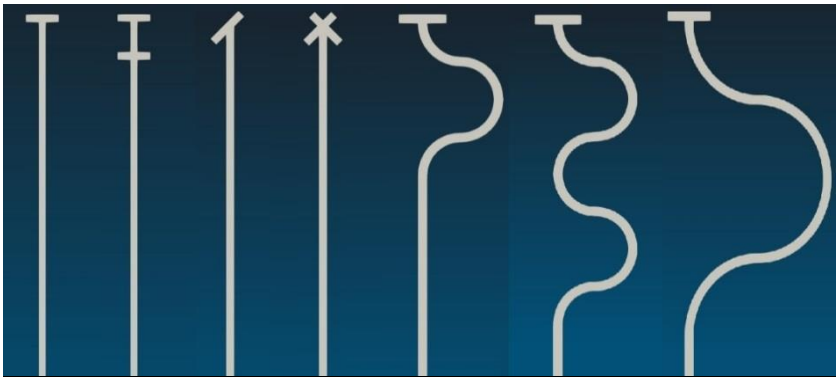

*Figure 23: The seven models that were studied – (001) plane.*

### 6.2.1. Discussion of the 2D Modelling Results

The results of the 2D modelling cases are the NMI's, 12.56 mm downstream of the mixing point. The NMI is an integral parameter that considers the entire field value *alpha* (the normalized standard deviation of the species fraction). As shown in table 11, the geometrical feature of two inlets per fluid has the most prominent enhancement in the mixing efficiency (~15%) as compared to the standard case of a simple "T".

Additionally, tilting the inlets improve the mixing over perpendicular ones by ~1%. Winding the mixing channel is the second most important feature, improving the mixing efficiency up to ~4%. In addition, the pressure drop along the mixing channel up to the point of NMI evaluation is reported for each geometry. The pressure drop per NMI accounts for the enhancement in mixing per increase in upstream pressure to drive the flow across the microfluidic. This parameter is important in quantifying the viscous heat generation.

Based on the above discussion, the geometrical features that will yield an efficient 3D microfluidic mixer are (in descending order): multiple inlets, winding the mixing channel, adding winding turns, and tilting the inlets to the mixing channel. These features will be combined in several 3D models for the accurate evaluation of the mixing time and length. It is important to note that the multiple inlets will inevitably have a variable pressure drop across each inlet which has to be accounted for in the HPLC pumps. The maximum pressure drop between inlets are ~0.2 bars.

*Table 11:The NMI and the pressure drop from the selected seven geometries.*

| Geometry | | | NMI | Δ* | ΔP** | NMI/ΔP |
|---|---|---|---|---|---|---|
| Inlets/Phase | Winding | Type | | | | |
| 1 | No | Tee | 0.838 | - | 2.23 | 0.38 |
| | | Wedge 45° | 0.847 | 1.0% | 2.43 | 0.35 |
| | Yes | N turns=2 R=2 mm | 0.860 | 2.6% | 2.56 | 0.34 |
| | | N turns=4 R=1 mm | 0.858 | 2.3% | 2.62 | 0.33 |
| | | N turns=8 R=1 mm | 0.872 | 4.0% | 2.67 | 0.33 |
| 2 | No | Tee | 0.960 | 14.5% | 2.35 | 0.41 |
| | | Wedge 45° | 0.967 | 15.3% | 2.67 | 0.36 |

* $(NMI-NMI_{TEE})/NMI_{Tee}$ ** $\Delta P - \Delta P_{Tee}$

## 6.3. 3D Modelling of the Microfluidic Mixers (Mixing Parameters)

The 2D models have given a qualitative measure of the effect of various geometrical features on the mixing enhancement. However, the choice of using more than one 3D model implementing the tested 2D features is that the initial 3D model showed a 3D flow nature that was believed to greatly affect the performance of the micromixer under investigation. The selected 3D models are: a simple-T (for comparison purpose), simple-tees with winding of the mixing channel (1 mm radius), and a triple-tee in which the HMUR is split into two inlets. The geometries of interest are listed in table 12. These features are known to be feasible from an industrial point of view, through surface etching.

Additionally, the effect of various parameters was investigated for the 1 mm winded geometry: doubling the flow rate, doubling the winding radius, and implementing the experimental uncertainties in the models. The uncertainties were implemented by reducing the diffusivity and increasing the viscosity with one standard deviation (chapter 5). The combined effect represents the least favorable combination as seen in Einstein-Stokes equation (Eq. 2). The flow rate is a variable parameter in the actual production where previously reported values can be up to three time the normal flow rate of the original models. Increasing the flow channel diameter is an option in etching the mixing channels.

The models implement the following features and modifications:

- An LES model of one eddy viscosity equation with boundary layer refinement
- An Additional feature of a reservoir to develop a parabolic velocity profile at the inlets. The micromixers are will be connected to reservoirs holding the feed solutions.
- Extending the models to 100 mm since the diffusivity is ~3 times less than that of water.
- Modelling the solutions at 15 °C, the diffusivity and viscosity values were interpolated using Einstein-Stokes equation (Eq. 32) and the logarithmic fit (Eq. 24), respectively.
- The reference geometry is the winded micromixer with the already utilized flow rate in previous gelation experiment [27].
- Implementing a refined mesh, the number of cell ranged between 1.7 million cells for the simple-T geometry to 2.6 million cells for the winded geometry.

*Table 12: The specifications of the six modelled microfluidic mixers. The winding radius is 1 mm except for the scaled geometry No 5, which equals 2 mm.*

| No | Geometry | Inlets | Winding | D- Mixing Channel (μm) | Flow Rate (mL/min) | Physical Constants |
|---|---|---|---|---|---|---|
| 1 | T | 2 | No | 250 | 3.2 | D, μ |
| 2 | T-Winding-1 | 2 | Yes | 250 | 3.2 | D, μ |
| 3 | T-Winding-2 | | | 250 | 3.2 | D-σ, μ+σ |
| 4 | T-Winding-3 | | | 250 | 6.4 | D, μ |
| 5 | T-Winding-4 | | | 500 | 12.8 | D, μ |
| 6 | Triple-T | 3 | No | 250 | 3.2 | D, μ |

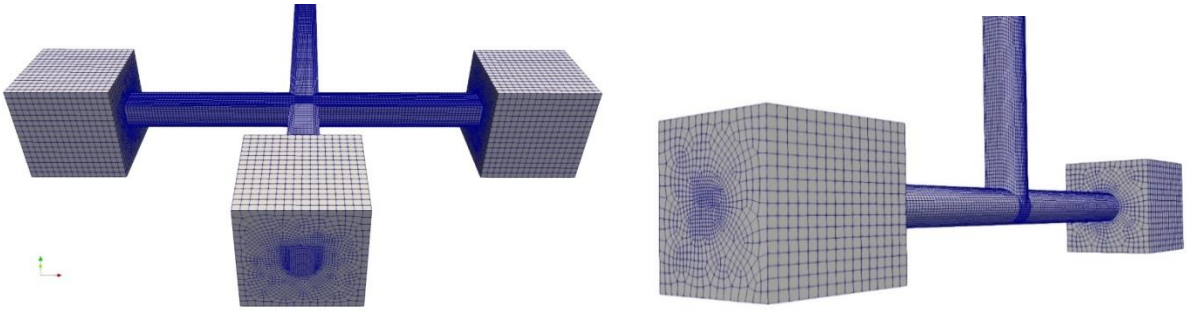

*Figure 24: The triple inlet micromixer (left, where the inlet of the metal solution is the middle, the HMUR is divided to two inlets) and the multiple inlets for the reference models.*

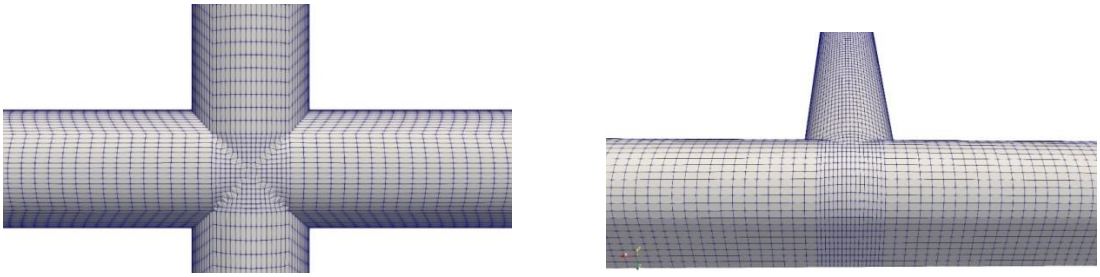

*Figure 25: The mixing zone of the triple inlet micromixer (top, where the inlet of the metal solution is the middle, the HMUR is divided to two inlets) and the multiple inlets.*

The dimensionless numbers of the modelled flow fields are listed in table 14. As expected, microfluidic mixers are characterized by a low Reynolds number, the flow is generally laminar while it can deviate locally depending on the velocity field. Péclet numbers show that the flow field in microfluidic mixers is advection dominated, the diffusion term is minimal (three orders of magnitude less in the case of local Péclet number). Péclet number is proportional to the ratio of the diffusion time to the residence time, and from Péclet numbers, all cases are expected to have equal diffusion times, except for the conservative case that will need ~25% more time for diffusion. While the diffusive term is concentration dependent, an enhancement to diffusivity is reached by increasing the interface area between the diffusing species. The convective term can be enhanced largely by creating flow fields of high convective nature, i.e., vortices. The effect of vortices is tested in the micromixers no 2, 3, and 4.

*Table 13: The dimensionless numbers governing the mixing phenomena.*

| No | Geometry | Reynolds No | Péclet No | Residence Time (ms) * |
|---|---|---|---|---|
| 1 | T | 41.2 | 3.8E5 | 104.6 |
| 2 | T-Winding-1 | 41.2 | 3.8E5 | 104.6 |
| 3 | T-Winding-2 | 40.7 | 5.2E5 | 104.6 |
| 4 | T-Winding-3 | 82.4 | 7.6E5 | 52.3 |
| 5 | T-Winding-4 | 329.5 | 3.0E5 | 104.6 |
| 6 | Triple-T | 41.2 | 3.8E5 | 104.6 |

** Residence time is the time it takes to the flow from the mixing point to 100 mm downstream the channel.*

### 6.3.1 Analysis of the 3D Micromixer Designs

The models were run until the steady state was reached, which is approximately the time it takes the species to go from the reservoir to the end of the mixing channel. Given that the mixing ratio is 1.55 to 1.00 from the HMUR to the CAN solution, a perfect mixing can be observed if the HMUR volume fraction reaches 0.608 across the mixing channel. Because that it not achieved in some geometries, two intervals of 1 $\sigma$ and 2 $\sigma$ were used to locate the length at which this mixing level is achieved, i.e., a volumetric fraction of HMUR of 0.623 and 0.638, respectively. By using these mixing lengths that ensure these levels of mixing (95% and 97.5%), mixing times were evaluated, as listed in table 14. The NMIs are also reported at the outlet (100 mm from the mixing point). At this point in the micromixer, it is difficult to assess the efficiency of mixing between various geometries, rather the mixing length and times are good measures of the geometrical and flow effects.

The simple-T geometry achieved the least strict mixing requirement at +9 cm, while the stringent requirement was not observed. Winding the mixing channel (radius of 1 mm) reduced the required mixing lengths and times by a factor of two. Implementing conservative physical constants slightly increased the mixing length and time. Doubling the flow rate has a dramatic improvement in the mixing length and especially the mixing time. The results showed improvements ~16% compared to that of the simple-T. Scaling the geometry (at the same flow rates downstream the mixing channel) has not satisfied any of the mixing requirement. Thus, the flow rate was increased four times, which resulted in poor mixing as compared to other geometries of up to +8 cm for the stringent mixing criteria. A multiple inlet micromixer has an efficiency comparable to that of a simple winding micromixer.

These observations are not scaling from the previous 2D results, where having multiple inlets geometry yielded the most efficient micromixer. However, the results of the 3D model show that winding has a dramatic mixing improvement. The winded mixing channels resulted in a 10% improvement in the mixing times and length as compared to the multiple inlets mixer. This is contradictory to the 2D result, mainly due to the 3D nature of the flow which amplifies the convection driven transport in the geometry that incorporates windings.

Additionally, the conservative model in which the diffusivity was reduced by ~35% (the maximum experimental error from combined diffusivity measurements) has showed an increase in the mixing length and times is less than 5%. This supports the argument that the mixing process is convection driven rather than diffusion driven, which also reduces the importance of the experimental uncertainties.

*Table 14: The mixing times and lengths to achieve the required mixing levels (-5.0% and -2.5%) from the perfectly mixed conditions.*

| No | Geometry | Time +5.0% (msec) | Time +2.5% (msec) | Length +5.0% (mm) | Length +2.5% (mm) | 100 mm NMI |
|---|---|---|---|---|---|---|
| 1 | T | 88.3 | NA* | 95.9 | NA* | 0.9987 |
| 2 | T-Winding-1 | 36.6 | 45.7 | 44.2 | 55.1 | ~1.0000 |
| 3 | T-Winding-2 | 38.9 | 47.6 | 47.0 | 57.5 | ~1.0000 |
| 4 | T-Winding-3 | 12.9 | 16.9 | 31.2 | 40.8 | ~1.0000 |
| 5 | T-Winding-4 | 52.6 | 68.7 | 63.5 | 82.9 | 0.9998 |
| 6 | Triple-T | 39.7 | 50.6 | 47.9 | 61.1 | ~1.0000 |

* Mixing level not observed in a 100 mm channel

The grid refinement at the wall boundary layer result in the y+ values that describe how well the boundary layer is resolved (where the the location of the grids first node is located in the viscous sublayer). The selected max/average y+ values are:

- Geometry No 4, winded-T with double the flow rate; 2.11/0.56
- Geometry No 6, triple-T; 1.29/0.40

### 6.3.2. Mixing Enhancement in Winded Micromixers

The winded geometries have very high efficiency mixing levels. Such effect is due to the secondary flow or "Prandtl flow of the second kind" [67] [68]. The primary flow field is the one parallel to the flow channel, while the secondary flow field is a flow perpendicular to the flow channel.

The two fluids in the micromixer have different properties. The metal solution is more dense (+31%), and slower (-35%) from the HMUR solution. The larger density tends to make the metal solution drift to the larger radii of a bend. From the results, it was observed that the CAN solution tended to drift to larger radii. The CAN will tend to flow aside the higher radius of the curve, and since the winding is repetitive, the CAN (and so the HMUR solution) will alternate between the two sides of the micromixer until being sufficiently mixed. Such behavior will induce a secondary flow field in the initial windings and enhance the convection term. Additionally, in shifting the location between two sides, between the windings the CAN will be approximately flowing inside the micromixer and surrounded by the HMUR solution from all sides. In such positions, interface area is maximum and higher diffusion currents and mixing will be encountered. Such effect is seen in figures 26, 27 and 39, and the mixing is enhanced further at higher flow speeds.

The Prandtl flow is dependent on the winding radii for a given flow speed and physical properties. Very large radii would mix the two fluids to a level that the speed deference may become independent. Additionally, the velocity difference between the inner and outer radii is smaller. On the other side, very narrow winding may not give enough time for the fluids to alternate between the radii of

different windings. For the current flow rates of 3.2 and 6.4 mL/min, the flow pattern was evident in both for a winding of 1 mm radius. The radius of 1 mm is recommended for the proposed microfluidic mixer at these flow conditions. A higher winding radius may enhance the phenomena (less than 2 mm radius, since this phenomenon diminished at this winding) which is recommended for further studies. Additionally, this phenomenon was not foreseen in the 2D models, since the Prandtl flow is a 3D flow field, and so, the effect of winding was absent in the 2D models.

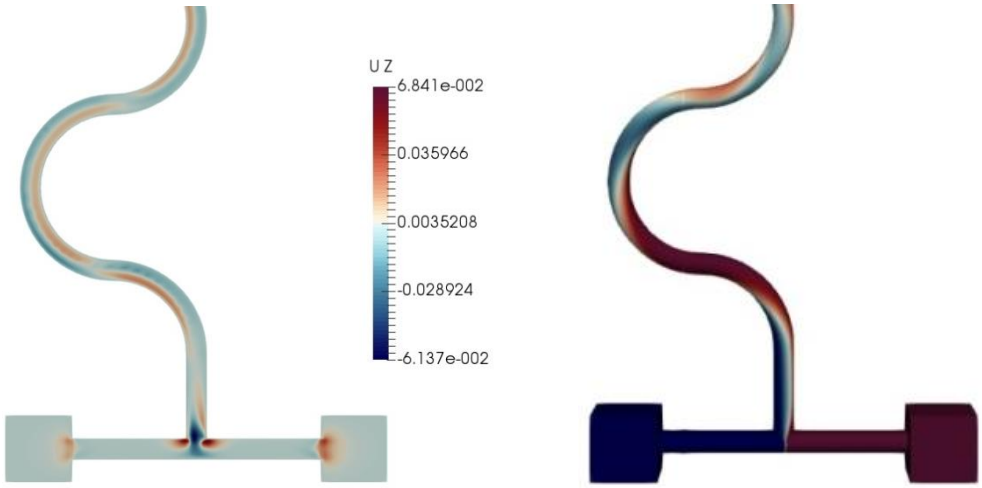


*Figure 26: The Prandtl flow is seen by observing the location of both solutions along the windings of the mixing channel (right), which shows the concentration of the solutions. The alternating behavior is not fully developed suggesting that higher winding radii may improve the mixing. Prandtl flow is a 3D phenomenon, in which an axial component of the velocity is induced in alternating pattern between the different windings (left).*

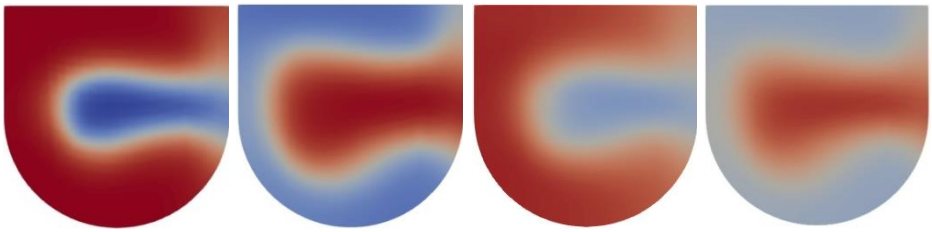

*Figure 27: Cross section view at the locations of winding direction change (first up to fourth change in winding direction), the CAN solution (blue) is alternatively shifting position to allocate itself around the high radius of the curvature and consequently displacing the slow HMUR solution.*

*Figure 28: Cross section view at the first winding shift: 6.4 mL/min. The HMUR is detaching the right wall (right), to position itself in a lower curvature, such displacement will create an axial velocity ahead of the moving solution, where it is positive (up) in the top left part, and negative (down) in the bottom left part.*

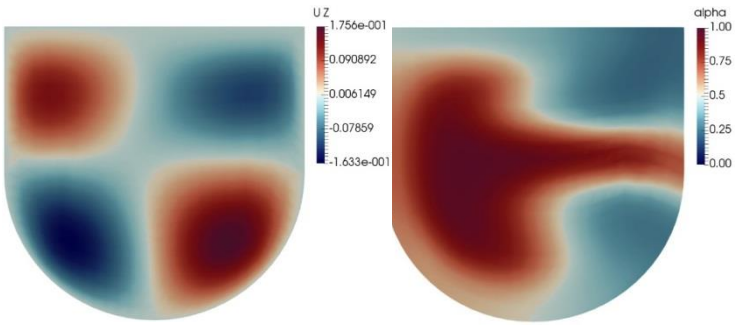

### 6.3.3. Mixing Enhancement in Multiple-Inlets Micromixers

Diffusion is governed by Fick's first law (equation 1), which is driven by the concentration gradient. The effect of having multiple inlets is that ***n-1*** interfaces are created, where ***n*** is the number of inlets. In the multiple-inlet case (here 3 inlets), two interfaces are formed in the mixing channel; hence the concentration gradient is twice as large as the two inlets cases. The two inlets are to be arranged in a staggered pattern so that each fluid is moving between regions of the other fluid (figure 29 and 30).

*Figure 29: The triple-inlet micromixer, where the "Red" represents the HMUR solution and the "Blue" represents the CAN solution.*

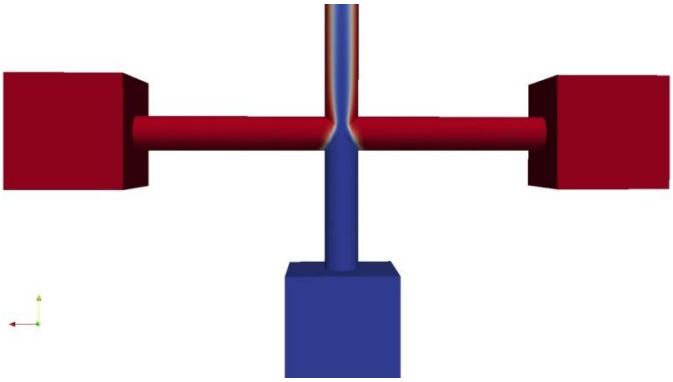

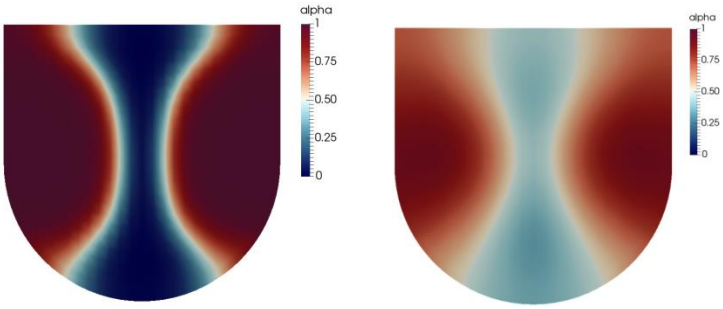


*Figure 30: A cross-sectional cut downstream the mixing channel in the triplet inlets micromixer. An initial sharp gradient (left) develops into a softened gradient (right).*

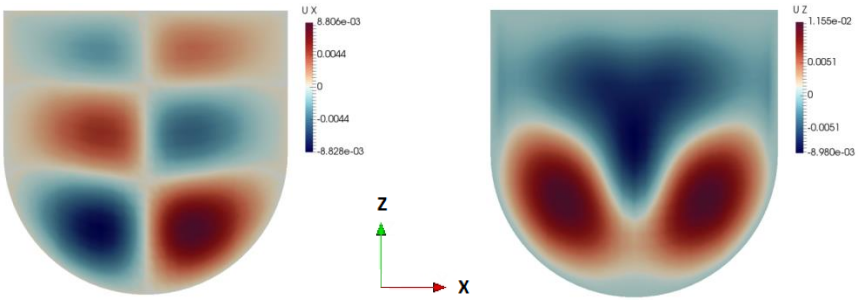


*Figure 31: A cross-sectional view of the downstream mixing channel of the triplet inlets micromixer. Initial vertically aligned interfaces are developing a curved shape by having a cross flow in the x and z directions.*

The modeled triple-inlet geometry has no winding, and it is expected that winding a triple inlets micromixer would not result in large enhancement. The lack of enhancement is expected because the

two fluids will be distributed according to the winding curvature, and alternate their position with winding direction, hence the original behavior in the winded geometry will be repeated. It is also observed that initially aligned interfaces are developing into curved ones, minimizing the wall contact area with the HMUR (the viscous fluid). Such re-alignment is achieved through cross flow in the x and z-directions as shown in figure 30.

### 6.3.4. The Mixing Levels Downstream the Mixing Channel

The progress of the NMI downstream the mixing channel from the mixing point was evaluated for the simple-T, winded-T, and the multiple-inlets geometries. The results of these models are shown in figure 32. The NMI does not representatively show the large improvements in the mixing efficiency of the modeled geometry, since the simple-T did not achieve one of the mixing criteria in the 100 mm mixing channel, while the two other models have the criteria achieved in less than 50 mm downstream the mixing channel. It is observed also that the winded geometry has step increases in the mixing levels, corresponding to each of the winding loops.

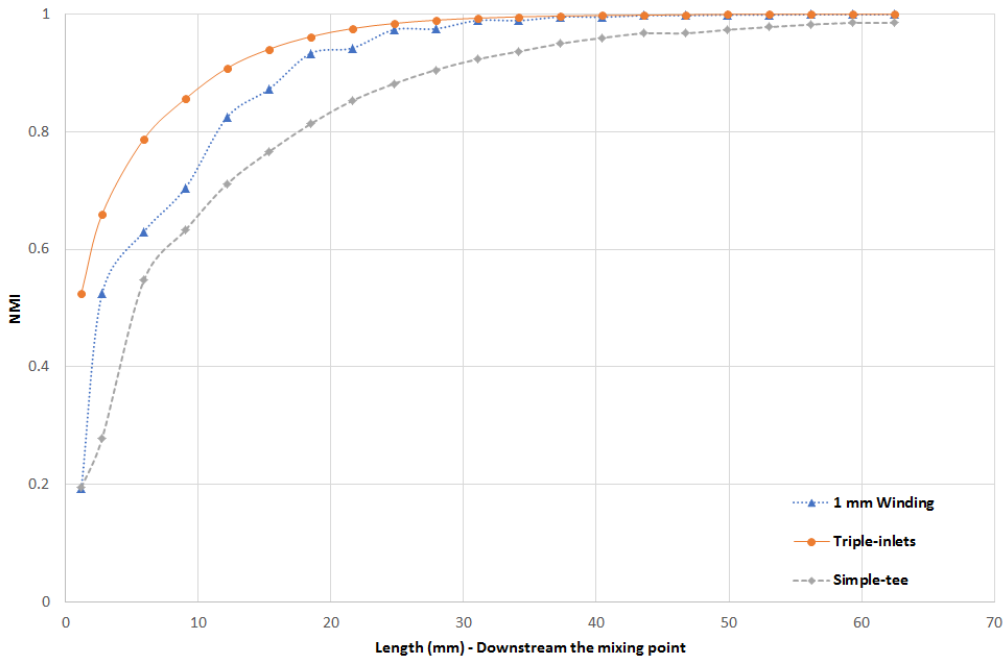


*Figure 32: The NMI downstream the mixing channels in three of the modeled cases – for the winding mode, each point corresponds to the transition from a loop to another.*

# Chapter 7. Modelling of the Droplet Generation Phenomenon

The approaches of rapid prototyping a 3D ceramic part include three dimensional printing (3DP) [24] and direct inkjet printing (DIP), and other approaches [25]. In the current study, the DIP approach is investigated. Direct inkjet printing can be achieved by using the continuous inkjet printing (CIP) and the drop-on-demand inkjet printing (DOD) [25] [28]. The former approach is investigated in the current study, since the later one includes additional moving parts in the flow channel (a piezoelectric actuator). This increases the possibility of flow stagnation, and hence, increases the chance of having permanently gelled oxides in the flow channels. The CIP is achieved through the continuous flow of the printing medium up to a printing nozzle, where droplet detachment occurs at a critical size, depending on the physical properties of the fluid (surface tension, contact angle, viscosity) and the flow parameters (flow rate, nozzle diameter, etc.). In addition, another mode in which the nozzle is mounted on an acoustic vibrator to enhance the droplets detachment is investigated. This mode of generating the droplets is termed “acoustic vibration” [30].

The phenomena connected to the additive pellet building process are not within the scope of the current study and hence, only the nozzle-related phenomena are studied. The investigated parameters are the volume of the detached droplets and the rate at which these droplets are being generated under two modes of operation, continuous uninterrupted flow and a vibrating nozzle head.

## 7.1. Specifications of the Inkjet Printing Head

The inkjet printing head (within the current study) is a needle that is similar to a previous project in PSI, in which the nozzle was mounted on a vibrator to generate a continuous stream of droplets [27]. The following are the properties of the fluids and the flow characteristics:

1. ***The solution:*** A fully mixed solution of the HMUR and the CAN solutions, with mixing ratio of 1.55/1.00, respectively, and a mixture density of 1282.4 Kg/m$^3$.
2. ***The mixture viscosity:*** The kinematic viscosity of the mixture is 6.84E-06 m$^2$/s and the dynamic viscosity is 8.77E-03 Pa.s (section 5.1). The mixture viscosity should not be represented as a linear function of the volumetric fractions as explained by Gambill [39]. However, the viscosity of the mixture was implemented as a linear function in the volumetric ratios of the constituents, as implemented in the *interFoam* model.
3. ***The mixture surface tension:*** (section 5.2): $\gamma = 69.22 \pm 0.43\ [mN.m^{-1}]$

4. ***The contact angle of the mixture and a stainless-steel surface:*** The models implement the contact angle of the CAN solution of 89.9° (section 5.3). This is assuming that the mixed solution will be enriched on the surface with the low surface tension component, or the CAN solution in this case. A case is also presented where the HMUR contact angle is used.
5. ***The needle geometry:*** The inner to outer diameters of the needle are 0.1 to 0.8 mm, respectively, as performed in a previous project [27].
6. ***The specifications of the vibrator:*** The shaker model v201 of the company Brüel & Kjær was implemented [69] according to a previous project in PSI [27]. The parameters of interest are:
    - Frequency: 13,000 Hz
    - Maximum acceleration sine peak: 91 g
    - Velocity sine peak: 1.83 m/s
    - Moving element mass: 0.020 kg

The acceleration and frequency of the shaker was corrected based on a mounted instrument (a printing head) with of a mass of 105.25 gm. Hence the effective acceleration is 142.53 m/s$^2$ and the effective frequency is 5200 Hz. Acceleration and frequency corrections are based on the mass of the shaker moving elements and the effective mass of a simple harmonic oscillator.

## 7.2. Physical Models of the Droplet Generation

For the CIP mode, the model does interface tracking, in which the OpenFOAM solver *interFoam* was utilized. The underlying equations of *interFoam* are described in section 3.2.2.

For the CIP-Vibrator mode the model also does an interface tracking that includes the vibration effect. For these models, two approaches were implemented :

1. ***A time varying external momentum source***

The *interFoam* solver was modified to depict the additional shaking action from the shaker by explicitly including a momentum source as a function of the simulation time. It is assumed that the shaking effect will result in an additional momentum source in Navier Stoke' s equation $\boldsymbol{F_{ext}(z)}$ :

$$\frac{\partial \rho U}{\partial t} + \nabla.(\rho U U) = -\nabla p + \nabla.\left(\mu_{eff}[\nabla U + (\nabla U)^T]\right) - \rho g + F_s + F_{ext}(z)$$

Where $\boldsymbol{F_{ext}(t)}$ is an explicitly defined volumetric force that is implemented as :

$$F_{ext}(t) = \rho.a_{SHO}$$

Where *m* is the oscillating mass (the shaker and the nozzle) and $a_{SHO}$ is an additional acceleration representing a simple harmonic oscillator:

$$a_{SHO} = a_{max}\, sin(2\pi.f\ t)$$

A new solver was compiled based on the *interFoam* solver, which has a modified velocity equation that includes a time varying external momentum source. The modification was done as following:

```
volScalarField Fext = rho*142.23*Foam::sin(2*3.1416*5200*runTime.value());

    fvVectorMatrix UEqn
    (
        fvm::ddt(rho, U)
      + fvm::div(rhoPhi, U)
      + turbulence->divDevRhoReff(rho, U)
      - Fext*g/mag(g.value())
    );

    UEqn.relax();
```

### 2. *A dynamically moving mesh*

The OpenFOAM solver *interDyMFoam* that supports a dynamic mesh was used and the model was divided into two zones, a stationary outlet, and a sinusoidally oscillating nozzle. The outlet and nozzle parts of the mesh are shown in figure 33. The dynamic motion was specified accordingly as:

```
dynamicFvMesh   solidBodyMotionFvMesh;
motionSolverLibs ( "libfvMotionSolvers.so" );
solidBodyMotionFvMeshCoeffs
{
    cellZone                                  Nozzle;
    solidBodyMotionFunction  oscillatingLinearMotion;
    oscillatingLinearMotionCoeffs
    {
        amplitude  (0 0.000012 0); // amplitude - µm
        omega      81700;          // angular frequency - rad/s
    }
}
```

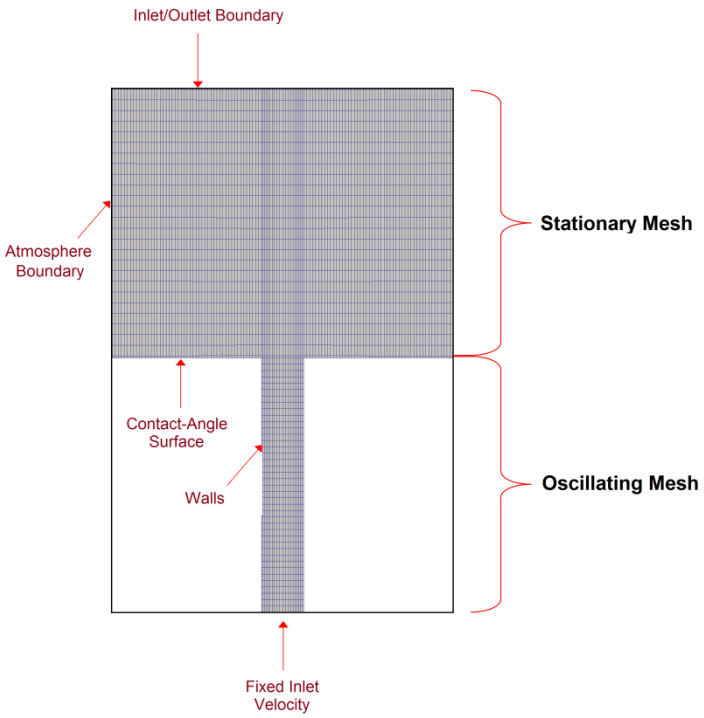


*Figure 33: The mesh of the 2D wedge geometry. The top section is the stationary mesh and the bottom is the dynamically oscillating mesh that represents an oscillating nozzle. The implemented boundary conditions are also shown.*

## 7.3. 2D Models of the Droplet Generation

The 3D results of the field values: velocity and volume fraction show radial symmetry. To evaluate the parameters of interest with a reasonable computing resources, 2D models were implemented. This was done to reduce the number of cells in the domain by two orders of magnitude, which reduced the computation time. In this case, the geometry is a "*Wedge*" in which the field values are constant in the radial direction (***Uz(θ) = constant***, and ***θ*** is the azimuthal in cylindrical coordinates). The OpenFOAM meshing utility *blockMesh* was used to create several 2D models that were later extruded into wedges.

The printing nozzle would be between 4 to 5 mm above the under-construction ceramic green part (stand-off distance). This space is required to be enough to generate the stream of droplets and also as short as possible, not to deteriorate the spatial resolution of the printing process. And so, the reference model resembles: an inlet boundary conditions of fixed inlet velocity through a nozzle (1.6 mL/min flow rate), a nozzle diameter of 100 µm, and a stand-off distance of a maximum of 5 mm.

The Reynolds number under this condition is 99, considering that the flow speed is 6.8 m/s. The hydrodynamic entry length is 496 µm which is the length of a hydrodynamic entry region that is necessary to result in a fully developed flow [70]:

$$L_{h-laminar} = 0.05\ Re\ D$$

A 1000 µm is sufficient to result in a fully developed flow.

Several parameters were investigated for their effects on the droplet generation time and volume, which includes: nozzle diameter, vibration frequency, vibration amplitude, and the solution flow rate. A graphical representation of the implemented parameters in the 2D models is shown in figure 34.

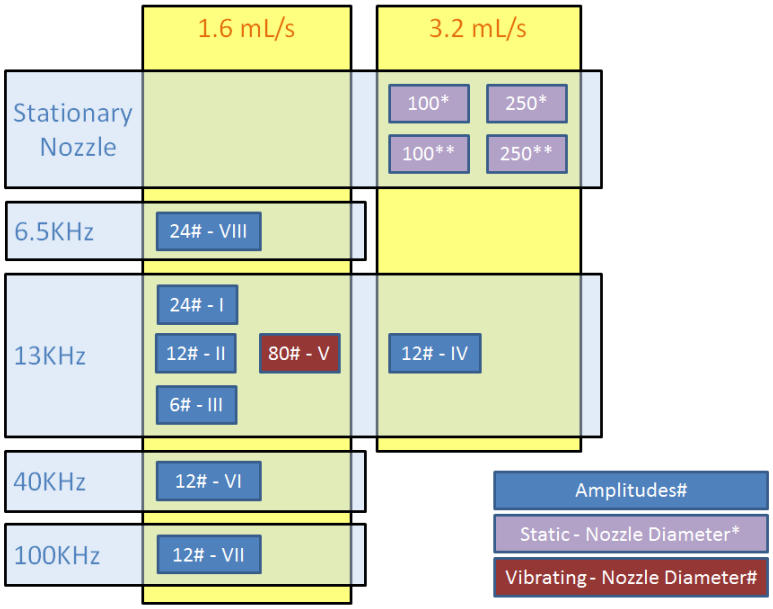


*Figure 34: The range of parameters that are studied in the 2D droplet generation models: the frequency (horizontal), and the flow rate (vertical) – all the dimensions are in µm. The eight cases of the vibrating nozzle are labeled with Roman numerals.*

## 7.4. The Results of the Droplet Generation Modelling

The parameters of interest from the droplet generation models are the droplet generation time and the average droplet diameter. The former constrains the available time for drying a droplet on the green body under-construction, or at least accelerating the gelation reaction to increase the viscosity of the printed fluids. The average droplet diameter is defining the overall spatial resolution of the printing process, and within the objective of building an internal structure in a fuel pellet, the obtained resolution should be ~100 μm. Additionally, the minimum stand-off distance from the green body that is required to generate the droplets is also investigated.

### 7.4.1. The Static Nozzles

Four cases were modeled as a static printing head: 100 and 250 μm nozzle diameters, using contact angles of 89.9° and 94.4° for each model. It is observed that the contact angle has no effect on the results, which are listed in table 15. The 100 μm diameter nozzle showed a non-steady breakup volume and time within the 10 mm distance from the nozzle. The 250 μm diameter nozzle showed Rayleigh instability for the liquid jet that eventually results in the jet breakup into droplets at ~8 mm below the nozzle, as shown in figure 35. Given the requirements of a high spatial resolution and a shorter stand-off distance, the static nozzles are not promising in the current application.

*Table 15: The break-up diameter and time for the static nozzles.*

| Nozzle Diameter (μm) | Break-up Diameter (μm) | Break-up time (ms) | Stand-off Distance (mm) |
|---|---|---|---|
| 100 | 460-520 | 0.96-13.8 | 8-9 |
| 250 | Irregular | - | 7 to >10 mm |

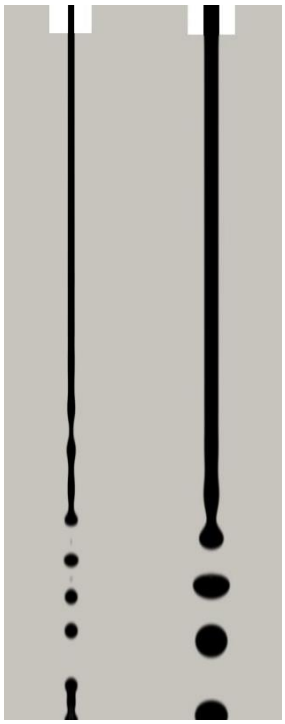

*Figure 35: Droplets break-up as modelled in OpenFOAM from 100 and 250 μm static nozzles. Note that the image is not to scale in the axial direction.*

### 7.4.2. The Vibrating Nozzles

The results of using a time varying gravity field were not satisfactory. A vacuum was observed in the nozzle channel and the behavior of the liquid jet depended on the upstream nozzle length. Consequently, this approach was not followed in further modelling of the vibrating nozzle. As shown in figure 36, eight cases were modeled as vibrating printing heads using the dynamic mesh solver *interDyMFoam*, mostly at the 13 kHz and 1.6 mL/min [27]. The results are listed in table 16.

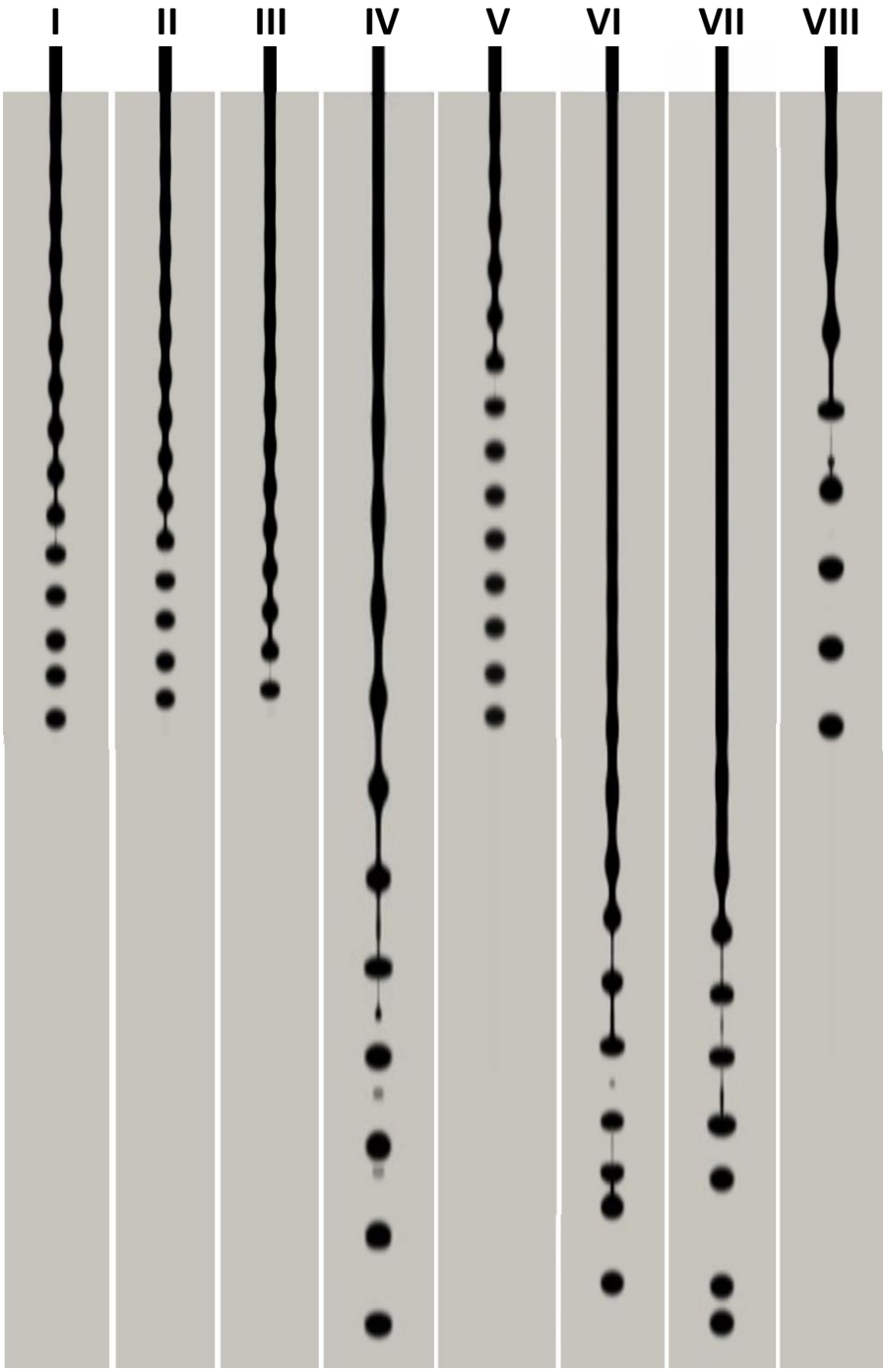


*Figure 36: Droplets break-up as modelled in OpenFOAM from a 100 µm vibrating nozzle. Cases I, II, III, V, and VIII were modeled up to 5 mm, and the remaining cases are up to 10 mm.*

*Table 16: The droplets break-up diameters, times and the nozzle stand-off distances for the vibrating models.*

| Case | Flow Rate (mL/min) | Vibration Amplitude (µm) | Vibration Frequency (kHz) | Break-up Diameter (µm) | Break-up time (ms) | Stand-off Distance (mm) |
|---|---|---|---|---|---|---|
| I | 1.6 | 24 | 13 | 160 | T | 3.4 |
| II | 1.6 | 12 | 13 | 160 | T | 3.6 |
| III | 1.6 | 6 | 13 | 160 | T | 4.6 |
| IV# | 3.2 | 12 | 13 | 200 | T | 6.0 - 6.5 |
| V* | 1.6 | 12 | 13 | 137 | T | 1.9 - 2.1 |
| VI# | 1.6 | 12 | 40 | Irregular | Irregular | 6 - 8 |
| VII# | 1.6 | 12 | 100 | Irregular | Irregular | 5 - 7 |
| VIII# | 1.6 | 24 | 6.5 | 200 | T | 2.5 - 3.0 |

** The minimum observed breakup diameters # Satellite droplets are observed*

The mentioned parameters were varied to test their effects on the droplets size, generation rate, and the nozzle stand-off distance. In the following comparison, case I is the reference case :

1. ***The effect of the vibration frequency:*** Increasing the vibration frequency as implemented in cases VI and VII up to 40 and 100 kHz deteriorated the quality of the droplets. The droplets had irregular size and they were generated at variable rates that did not follow the imposed frequencies. Satellite droplets were observed too. On the other hand, decreasing the frequency in case VIII resulted in a regular droplet generation rate that followed the imposed frequency. Yet, since this frequency is half that of the reference case, the generated droplets are ~25% larger in diameters. These models were investigated up to 10 mm too.
2. ***The effect of the flow rate:*** Increasing the flow rate as implemented in case IV resulted in a larger droplets size too. Since the droplets will be generated according to the imposed frequency, and in the same period, the fluid volume exiting the nozzle doubled, resulting in a droplet size that is 25% more than the reference case. Additionally, the breakup happened at a delayed distance from the needle tip, approximately double the value of the reference case. Hence, this model was investigated up to 10 mm as well.
3. ***The effect of the vibration amplitude:*** Reducing the amplitude by 2 and 4 folds did not significantly change the results. The droplets were generated at the same rate and size, but at slightly larger distances. The effect of the vibrator amplitude can be seen in these cases to create a periodic disturbance on the ejected fluid column that develops a Rayleigh instability and an onset of breakup. The importance of the insensitivity to the vibration amplitude is to have flexibility in mounting heavier printing heads on the shaker nozzle.
4. ***The effect of the nozzle diameter:*** The most promising result, in terms of the resolution of the 3D printing, is the 80 µm nozzle diameter case. Since the breakup happens at the rate of the vibration, the ejected volume is smaller, and hence the droplet size as well. Also, the minimum stand-off distance corresponds to this model, which is recommended for the design phase.

# Chapter 8. Summary of The Design Parameters of the 3D Printing Head

Based on the previous results and discussions regarding the mixing in microfluidic mixers and the droplet generation from a printing head, the following points are the proposed design parameters of the 3D printing head :

1- An upstream passive mixing microfluidic mixer. The geometry of the mixing channel should implement a winding pattern of 1 to 2 mm radius. Another approach is to split the HMUR inlet into two inlets that enclose the CAN solution inlet. The two geometrical effects should not be combined. The valid flow rates are between 3.2 – 6.4 mL/min. Given these conditions, ~60 mm length of the mixing channel should result in ~97.5% mixing level of the two fluids under the scope of the current study at 15 °C.

2- A downstream printing head, which is a needle with 80 μm inner diameter. The flow rate through the needle should be between 1.6 to 3.2 mL/min for optimum parameters of the droplets. The needle shall be mounted on an acoustic shaker that has a frequency range between 6.5 to 13 kHz, and an amplitude range between 6 to 24 μm. Higher flow rates and higher frequencies should be avoided.

The above mentioned parameters can be used as guidelines for designing a printing station which generates a continuous stream of the internal gelation feed solutions in the fully mixed condition in a micro-metric size droplets, that will be deposited on the under-fabrication nuclear fuel pellet.

# Chapter 9. Conclusions

The current study is an initial approach to optimize upfront stages of a proposed technique for manufacturing nuclear fuels through combining an aqueous oxide production method (internal gelation) and an additive manufacturing technique (3D ceramic printing). The two stages that are the scope of the current study are :

1- Mixing of the feed solutions for the internal gelation process (the CAN and the HMUR solutions)
2- Droplets generation from a printing head

The optimization parameters of the mixing and droplet generation stages included the minimum mixing length and time, and the droplet size and generation rate. CFD models were created using several meshing tools and solved using the OpenFOAM software which represent the proposed microfluidic mixers and the printing nozzle.

In the mixing models, the mixing phenomenon was investigated based on 3D models that implement geometrical features that are industrially feasible to study their mixing enhancement. The features of interest are winding of the mixing channel, and splitting at least one of the feed solutions through two inlets. Both approaches resulted in satisfactory mixing lengths and times of about ~60 mm and 50 ms. The winding geometrical feature has shown the Prandtl flow of the second kind, in which the CAN solution is alternating its position along the mixing channel aligning itself near the large radii of the curvatures. The split inlet feature has shown an increase of the interfacial contact area between the two feed solutions. Both effects have largely enhanced the required mixing times. While the split inlet feature could be extrapolated to further decrease the mixing time, the winding feature is thought to be closely linked to the flow rates and the winding radii, and the recommended ranges are discussed in chapter 8.

In the droplets generation models, the optimization parameter are the generation rate, droplet size and the stand-off distance of a printing nozzle. These parameters were optimized to improve the spatial resolution of the 3D printing process, and to have a better control over the generated droplets. A first conclusion is that static nozzles will not fulfill the target of producing sufficient small droplets, therefore the acoustically shaken ones are proposed instead. For this purpose, 2D axisymmetric models were created using OpenFOAM in a moving mesh. From the investigation, the recommended variables are to reduce the nozzle inner diameter up to 80 μm, and to maintain a vibration frequency within the range of 6.5 to 13 kHz. The investigated parameters showed less sensitivity to the vibration amplitude, which gives more flexibility in mounting heavier nozzles on the available acoustic shakers.

In order to simulate both stages and the connected phenomena, the properties of the fluids had to be measured. Firstly, the rheology showed Newtonian characteristics. The surface tension and the contact angle had large experimental uncertainties, however the implementation in the models did not result in a variation of the investigated parameters. Lastly, the diffusivity of the CAN solution into the HMUR solution was measured using the Taylor dispersion analysis. Given that these solutions are multispecies, polydisperse diffusivity was observed. The TDA setup was modified by making the mono-species solution in the background and the multi-species solution as solute. Then the different dilution patterns were measured in the background solution. The traditional Gaussians fitting approach was possible with this setup, and the results were compared to the width-height fitting approach. The models have shown low sensitivity to the implemented uncertainties of the measured diffusion coefficients. The low sensitivity is mainly due to the convection dominant transport in the proposed micromixers.

The conducted study has limitations that affect the interpretation of the results and the range of their validity. Firstly, the validation of the mixing models was not successful, as explained in section 6.2. Mainly, geometrical features in the reference experiments of the validation case have changed the flow such that it could not be implemented in the current models. However, the current physical model that implement a turbulence model (LES) instead of a laminar model is believed to be more representative, given the observations of the flow fields that resulted from the initial modelling cases.

Even though the 2D models for the mixing phenomena were conducted in the current study to select between different geometrical features which enhance the mixing performance of a micromixer. The 2D models does not represent the phenomena of mixing two fluids with different velocities, densities, and viscosities. The flow fields have a 3D nature. These limitations in the 2D models showed the necessity to investigate the effects of the geometrical features in various 3D models.

The droplet generation is not validated. It was not possible within the scope of the current work to validate the droplet generation modes. It was only concluded that the nozzle will generate droplets of the same number of vibrations from a 13 kHz vibrator at flow rate of 3.2 mL/min from a 100 μm nozzle [27]. The breakup rate is only validated in the current models, while the phenomenon behind the breakup was not validated. The droplet breakup was seen to develop from a Rayleigh instability downstream the ejected liquid column, the availability of photographs would later assess this result, since the break up from Rayleigh instability will happen downstream the ejection point and not directly on the needle.

The results and the supporting discussion are limited to the cerium ammonium nitrate solution. The CAN solution is used as a substitute for the uranyl nitrate in the internal gelation experiments. Therefore, the current results are only valid for a mock-up 3D printer that could be done to assess the technological feasibility.

Based on this discussion, the recommended future work should include : additional diffusivity measurements to reduce the experimental errors and to test the implemented fitting approach in the current study. Additionally, the uranyl solution should be characterized, so that the industrial production parameters could be established too. Validating the mixing models with more reliable experimental values is also essential. Validating of the droplet generation models is also required by investigating the breakup distance from the nozzle to confirm the Rayleigh instability observations.

Additionally, the heating effect of actinides loading on feed solutions prior to the intended gelation should be investigated. The localized heating from alpha decay is due to plotunium-238 and curium-252 which are part of the nuclide vector that is proposed for Gen IV nuclear fuels. The tracks of alpha in the broth can be evaluated using a suitable Monte Carlo code (SRIM [71]), and from which the energy deposition per track length can be evaluated. The fluid properties like the thermal conductivity and specific heat can then be used to numerically evaluate the time development of the temperatures in specific volumes that are large enough to sustain the gelation reaction using a software like OpenFOAM.

Regarding the overall process, the next downstream stage shall be thoroughly investigated to study the appropriate approaches to wash and clean the deposited droplets, while maintaining geometrical stability.

# References


[1] M. A. Pouchon and M. Streit, "3D ceramic printing of nuclear fuel," *PSI-TM-46-16-04,* 2016.

[2] M. A. Pouchon, "Aqueous additive production method for the fabrication of ceramic and/or metallic bodies". Switzerland Patent 17581EP, 2016.

[3] F. W. v. d. Brugghens, A. J. Noothout, M. E. A. Hermans, J. B. W. Kanij and O. Votocek, "A U(VI)-Process for Microsphere Production," in *CONF-700502, U.S. Atomic Energy Commission*, Gatlinburg, Tennessee, May 4–7, 1970.

[4] J. L. Collins and A. Chi, "Determination of Ideal Broth Formulations Needed to Prepare Hydrous Cerium Oxide Microspheres Hydrous Cerium Oxide Microspheres," Oak Ridge National Laboratory, ORNL/TM-2006/122, 2008.

[5] P. A. Haas, J. M. Begovich, A. D. Ryon and S. J. Vavruska, "Chemical Flowsheet for Preparing Urania Spheres by Internal Gelation," Oak Ridge National Laboratory, ORNL/TM-6850, Oak Ridge,, July 1979.

[6] J. L. Collins, R. D. Hunt, G. D. D. Cul and D. F. Williams, "Production of Depleted UO2 Kernels for the Advanced Gas-Cooled Reactor Program for Use in TRISO Coating Development," Oak Ridge National Laboratory, ORNL/TM-2004/123, December 2004.

[7] M. H. Lloyd, J. L. Collins, R. L. Fellows, S. E. Shell, D. H. Newman and W. B. Stines, "A Gel Sphere Process for FBR Fuel Fabrication from Coprocessed Feed,," Oak Ridge National Laboratory, Oak Ridge, ORNL/TM-8399, February 1983.

[8] M. Cabanes-Sempere, C. Cozzo, S. Vaucher, J. Catalá-Civera and M. Pouchon, "Innovative production of nuclear fuel by microwave internal gelation:," *Progress in Nuclear Energy,* vol. 57, pp. 111-116, 2012.

[9] J. L. Collins, M. F. Lloyd and R. L. Fellows, "The Basic Chemistry Involved in the Internal-Gelation Method of Precipitating Uranium as Determined by pH Measurements," *Radiochim. Acta,* vol. 42, pp. 121-134, 1987.

[10] S. H. Wong, M. C. Ward and C. W. Wharton, "Micro T-mixer as a rapid mixing micromixer," *Sensors and Actuators,* vol. 100, p. 359–379, 2004.

[11] C.-Y. Lee, C.-L. Chang, Y.-N. Wang and L.-M. Fu, "Microfluidic Mixing: A Review," *Int. J. Mol. Sci.,* vol. 12, pp. 3263-3287, 2011.

[12] A. Fick, "Ueber Diffusion," *Ann. der Physik (in German),* vol. 94, no. doi:10.1002/andp.18551700105, pp. 59-86, 1855.

[13] J. Branebjerg, "From microfluidic components to micro-TAS," in *In Proceedings of Micro Total Analysis System Workshop*, Enschede, The Netherlands, 21–22 November 1994.

[14] L. Scampavia, G. Blankenstein, J. Ruzicka and G. Christian, "A coaxial jet mixer for rapid kinetic analysis for chemical and biological microreactors," *Anal. Chem.,* vol. 67, p. 2743–2749, 1995.

[15] D. Beebe, R. Adrian, M. Olsen, M. Stremler and B. J. H. Aref, "Passive mixing in microchannels: fabrication and flow experiments," *Mec. Ind.,* vol. 2, p. 343–348, 2001.

[16] A. Bertsch, S. Heimgartner, P. Cousseau and P. Renaud, "Static micromixers based on large-scale industrial mixer geometry," *Lab Chip,* vol. 1, pp. 56-60, 2001.

[17] S. H. Wong, P. Bryant, M. Ward and C. Wharton, "Investigation of mixing in a cross-shaped micromixer with static mixing elements for reaction kinetics studies," *Sensors and Actuators,* vol. 95, no. B, pp. 414-424, 2003.

[18] T. Veenstra, T. Lammerink, M. Elwenspoek and A. v. d. Berg, "Characterization method for a new diffusion mixer applicable," *J. Micromech. Microeng.,* vol. 9, pp. 199-202, 199.

[19] A. Hashmi and J. Xu, "On the Quantification of Mixing in Microfluidics," *Journal of Laboratory Automation,* vol. 19, no. 5, p. 488–491, 2014.

[20] "Siemens sets milestone with first 3D-printed part operating in nuclear power plant," Siemens, 9 3 2017. [Online]. Available: https://www.siemens.com/press/.

[21] E. Sachs, M. Cima, P. Williams, D. Brancazio and J. Cornie, "Three dimensional printing: Rapid tooling and prototypes directly from a CAD model," *J. Manuf. Sci. Eng.,* vol. 144, no. 4, pp. 481-488, 1992.

[22] Q. Xiang, J. Evans, M. Edirisinghe and P. Blazdell, "Solid freeforming of ceramics using a drop-on-demand jet printer," *Proc. Inst. Mech. Eng. J. Eng. Manuf.,* vol. 211, no. 3, pp. 211-214, 1997.

[23] H. Shao, D. oZhao, T. Lin, J. huangHe and J. Wu, "3D gel-printing of zirconia ceramic parts," *Ceramics International,* no. In Press, Corrected Proof, 2017.

[24] E. Sachs, M. Cima, P. Williams, D. Brancazio and J. Cornie, "Three dimensional pPrinting: Rapid tooling and prototypes directly from a CAD model," *J. Eng. Ind.,* vol. 114, no. 4, pp. 481-488, 1992.

[25] B. Derby, "Additive Manufacture of Ceramics Components by Inkjet Printing," *Engineering,* vol. 1, no. 1, pp. 113-123, 2015.

[26] K. Seerden, N. Reis, J. Evans, P. Grant, J. Halloran and B. Derby, "Ink-jet printing of wax-based

alumina suspensions," *J. Am. Ceram. Soc.,* vol. 84, no. 11, pp. 2514-2520, 2001.

[27] M. A. Pouchon, "PINE - platform for innovative nuclear fuels," CCEM - Annual Activity Report, 2010.

[28] P. Blazdell and J. Evans, "Application of a continuous ink jet printer to solid freeforming of ceramics," *J. Mater. Process. Technol.,* vol. 99, pp. 94-102, 2000.

[29] B. Derby, "Inkjet Printing of Functional and Structural Materials: Fluid Property Requirements, Feature Stability, and Resolution," *The Annual Review of Materials Research,* vol. 40, pp. 395-414, 2010.

[30] H. Liu, Science and Engineering of Droplets:: Fundamentals and Applications (Materials and Processing Technology) 1st Edition, William Andrew, 2000.

[31] OpenCFD Ltd., [Online]. Available: http://www.openfoam.com/. [Accessed 1 8 2017].

[32] The OpenFOAM Foundation, [Online]. Available: https://openfoam.org/. [Accessed 1 August 2017].

[33] OPEN CASCADE, [Online]. Available: http://www.salome-platform.org/. [Accessed 1 8 2017].

[34] "csimsoft | Trelis Meshing Pre-processor," CSIMSOFT, [Online]. Available: http://www.csimsoft.com/trelis. [Accessed 15 August 2017].

[35] "OpenFOAM v5 User Guide: 5.3 Mesh generation with blockMesh - CFD Direct," CFD Direct, [Online]. Available: https://cfd.direct/openfoam/user-guide/blockmesh/.

[36] "OpenFOAM v5 User Guide: 6.1 ParaView / paraFoam - CFD Direct," CFD Direct, [Online]. Available: https://cfd.direct/openfoam/user-guide/paraview/.

[37] O. Penttinen, E. Yasari and H. Nilsson, *A pimpleFoam tutorial for channel flow, with respect to different LES models,* A course at Chalmers University of Technology, November 4, 2011.

[38] E. d. Villiers, *The Potential of Large Eddy Simulation for the Modeling of Wall Bounded Flows,* PhD Thesis, Imperial College of Science, 25th July 2006.

[39] W. Gambill, "How to estimate mixtures viscosities," *Chemical Engineering,* vol. 66, no. 5, pp. 151-152, 1959.

[40] O. Reynolds, "On the Theory of Lubrication and Its Application to Mr. Beauchamp Tower's Experiments, Including an Experimental Determination of the Viscosity of Olive Oil," *Phil. Trans. R. Soc. Lond.,* vol. 177, pp. 157-234, 1886.

[41] J. G. Eberhart, "The Surface Tension of Binary Liquid Mixtures," *J. Phys. Chem.,* vol. 70, no. 4, pp. 1183-1186, 1966.

[42] L. Eötvös, "Ueber den Zusammenhang der Oberflächenspannung der Flüssigkeiten mit ihrem Molecularvolumen," *Annalen der Physik,* vol. 27, p. 448–459, 1886.

[43] S. R. Palit, "Thermodynamic Interpretation of the Eötvös Constant," *Nature,* vol. 177, p. 1180, 1956.

[44] J. Snoeijer and B. Andreotti, *Phys. Fluids,* vol. 20, no. 057101, 2008.

[45] D. Li and A. Neumann, in *Applied Surface Thermodynamics*, New York, Dekker, 1996, p. 109.

[46] R. Tadmor, "Line energy and the relation between advancing, receding, and Young contact angles," *Langmuir,* vol. 20, no. 18, pp. 7659-64, 2004.

[47] C. EL., Diffusion: Mass Transfer in Fluid Systems, New York: Cambridge, 2009.

[48] B. Alder, D. M. Gass and T. E. Wainwright, *J. Chem. Phys.,* vol. 53, p. 3813, 1970.

[49] A. Alizadeh, C. A. N. d. Castro and W. A. Wakeham, "The Theory of the Taylor Dispersion Technique for Liquid Diffusivity Measurements," *International Journal of Thermophysics,* vol. 1, no. 3, 1980.

[50] A. A. AUzadeh and W. A. Wakeham, "Mutual Diffusion Coefficients for Binary Mixtures of Normal Alkanes," *International Journal of Thermophysics,* vol. 3, no. 4, 1982.

[51] G. Taylor, *Proc. Roy. Soc.,* vol. A219:186, 1953.

[52] A. R., "On the dispersion of a solute in a fluid flowing through a tube," *Proc R Soc London A.,* vol. 235, p. 67–77, 1956.

[53] M. Ghanavati, H. Hassanzadeh and J. Abedi, "Application of Taylor Dispersion Technique to Measure Mutual Diffusion Coefficient in Hexane + Bitumen System," *Wiley Online Library,* vol. 60, no. 7, July 2014.

[54] E. C and A. A., "Taylor Dispersion," *IUPAC Volume on the Measurement of Transport Properties of Fluids; Wakeham, W. A., Nagashima, A., Sengers, J. V., Eds.; Blackwell Scientific Publications: London,* pp. 251-265, 1991.

[55] A. R., "On the dispersion of a solute in a fluid flowing through a tube," *Proc R Soc London,* vol. 235, p. 67–77, 1956.

[56] C. R. and L. DG., "Diffusion coefficients for binary, ternary, and polydisperse solutions from peak-width analysis of Taylor dispersion," *J Solution Chem.,* vol. 35, p. 353–379, 2006.

[57] C. Secuianu, G. C. Maitland, J. P. M. Trusler and W. A. Wakeham, "Mutual Diffusion Coefficients of Aqueous KCl at High Pressures Measured by the Taylor Dispersion Method," *J. Chem. Eng. Data,* vol. 56, no. 12, p. 4840–4848, 2011.

[58] B. W. and K. H., "Measurements of diffusivities in liquids by the dispersion methods," *Chem Eng Sci.,* vol. 38, p. 1031–1037, 1983.

[59] "ActiPix™ D100 Software Manual v1.2," ActiPix™ , [Online]. Available: http://www.paraytec.com/downloads/manuals/. [Accessed 25 April 2017].

[60] O. Levenspiel and W. K. Smith, "Notes on the diffusion-type model for the longitudinal mixing of fluids in flow," *Chem. Eng. Sci.,* vol. 6, pp. 227-233, 1957.

[61] A. Einstein, "Über die von der molekularkinetischen Theorie der Wärme geforderte Bewegung von in ruhenden Flüssigkeiten suspendierten Teilchen". Annalen der Physik (in German)," *Annalen der Physik,* vol. 322, no. 8, p. 549–560, 1905.

[62] E. Cussler, in *Diffusion: Mass Transfer in Fluid Systems*, Cambridge, Cambridge University Press, 1984, pp. 15-54 (Chapter 2).

[63] N. Kockmann, C. Föll and P. Woias, "Flow regimes and mass transfer characteristics in static micro mixers," *Proc. SPIE,* vol. 4982, pp. 319-329, 2003.

[64] M. Hoffmann, N. Raebiger, M. Schlueter, S. Blazy, D. Bothe, C.Stemich and A. Warnecke, "Experimental and numerical investigations of T-shaped micromixers," in *Proc. of the 11th European Conference on Mixing*, Bamberg, Germany, 2003.

[65] V. Mengeaud, J. Josserand and H. Girault, "Mixing processes in a zigzag microchannel: finite element simulations and optical study," *Anal. Chem.,* vol. 74, p. 4279–4286, 2002.

[66] M. Yi and H. Bau, "The kinematics of bend-induced mixing in microconduits," *Int. J. Heat Fluid Flow,* vol. 24, pp. 645-656, 2003.

[67] L. Prandtl, Essentials of Fluid Dynamics, London: Blackie and Son Ltd., 1952 - pp 145-148.

[68] J. Piquet, Turbulent Flows: Models and Physics, Springer, 2001.

[69] "LDS V201 - Permanent Magnet Shaker," Brüel & Kjær, [Online]. Available: https://www.bksv.com/en/products/shakers-and-exciters/LDS-shaker-systems/permanent-magnet-shakers/V201. [Accessed 1 August 2017].

[70] B. T. L. and I. F. P., Fundamentals of heat and mass transfer, Wiley. ISBN 9780470501979, 2011.

[71] "SRIM - The Stopping and Range of Ions in Matter," [Online]. Available: http://www.srim.org/. [Accessed 15 8 2017].

[72] J. H. Ferziger and M. Peric, Computational Methods for Fluid Dynamics, ., rev. ed. - Berlin; Heidelberg; New York; Barcelona; Hong Kong; London; Milan; Paris; Tokyo - ISBN 3-540-42074-6: Springer, 2002.

[73] D. Junca and D. Ribeaute, Comment rédiger les bibliographies, Paris: Adventure Works Press, 2006.

[74] M. Beaud, Comment préparer et rédiger un mémoire de master, une thèse de doctorat ou tout autre travail universitaire à l'ère du Net, Grands repères, 2006.

[75] J.-F. Rieu, Rédigez efficacement vos rapports et thèses, ENI, 2012.

[76] A. Goguel d'Allondans, S. Boutillier, D. Uzunidis and N. Labère, Méthodologie de la thèse et du mémoire, Studyrama - Vocatis , 2012.